Motion Estimation and Compensation in Automotive MIMO SAR

Marco Manzoni, *Member, IEEE,* Dario Tagliaferri, *Member, IEEE,* Marco Rizzi, *Student Member, IEEE,* Stefano Tebaldini, *Senior Member, IEEE,* Andrea Virgilio Monti Guarnieri, *Senior Member, IEEE,* Claudio Maria Prati, Monica Nicoli, *Member, IEEE,* Ivan Russo, Sergi Duque, Christian Mazzucco, Umberto Spagnolini, *Senior Member, IEEE*

***Abstract*—With the advent of self-driving vehicles, autonomous driving systems will have to rely on a vast number of heterogeneous sensors to perform dynamic perception of the surrounding environment. Synthetic Aperture Radar (SAR) systems increase the resolution of conventional mass-market radars by exploiting the vehicle's ego-motion, requiring very accurate knowledge of the trajectory, usually not compatible with automotive-grade navigation systems. In this setting, radar data are typically used to refine the navigation-based trajectory estimation with so-called *autofocus* algorithms. Although widely used in remote sensing applications, where the timeliness of the imaging is not an issue, autofocus in automotive scenarios calls for simple yet effective processing options to enable real-time environment imaging. This paper aims at providing a comprehensive theoretical and experimental analysis of the autofocus *requirements* in typical automotive scenarios. We analytically derive the effects of navigation-induced trajectory estimation errors on SAR imaging, in terms of defocusing and wrong targets' localization. Then, we propose a motion estimation and compensation workflow tailored to automotive applications, leveraging a set of stationary Ground Control Points (GCPs) in the low-resolution radar images (before SAR focusing). We theoretically discuss the impact of the GCPs position and focusing height on SAR imaging, highlighting common pitfalls and possible countermeasures. Finally, we show the effectiveness of the proposed technique employing experimental data gathered during open road campaign by a 77 GHz multiple-input multiple-output radar mounted in a forward-looking configuration.**

***Index Terms*—SAR, Automotive, MIMO, Autofocus, Motion compensation.**

I. Introduction

The evolution to fully-autonomous vehicles requires the usage of a huge and heterogeneous set of sensors, such as cameras, LiDARs, radars, acoustic, etc., to enable advanced environmental perception [1]. Cameras and LiDARs are, respectively, passive and active optical sensors able to create high-resolution images and/or point clouds of the surrounding. If properly integrated, they can provide the vehicles with the capability of detect and classify objects in the environment. Automotive-legacy Multiple-Input Multiple-Output (MIMO) radars working in W-band ($76-81$ GHz [2]) are widely employed to obtain measurements of radial distance, velocity and angular position of remote targets [3]. Advantages of radars are more than a few: they work in any weather condition, do not need any external source of illumination and are available at low cost. However, mass-market automotive radars are characterized by a poor trade-off between angular resolution - typically above 1 deg -, range, bandwidth and Field Of View (FOV), challenging their usage for high-resolution environment mapping in automated driving [2], [4].

Significant effort was spent in recent works to increase the accuracy of environmental perception by means of Synthetic Aperture Radar (SAR) techniques [5]–[9]. With SAR, a moving radar sensor is employed to synthesize a large antenna array (synthetic aperture) by coherently combining different acquisitions in different positions of the trajectory; the range resolution, dictated by the bandwidth, remains the same as for conventional real aperture radars, while the angular resolution increases proportionally to the length of the synthetic aperture (typically $\ll 1$ deg). In [5], an automotive SAR system has been simulated using a radar mounted on a sliding rail. In [6], a 77 GHz radar with 1 GHz of bandwidth was mounted on the rooftop of a car to obtain images with resolution as small as 15 cm. The system proved to be capable of imaging the scene composed by cars, fences, sidewalks, houses and more. In [7] and [8], SAR images were used to search for free parking areas, while a 300 GHz SAR implementation (with 40 GHz of bandwidth) is presented in [9], showing millimeter-accurate imaging capabilities on a slowly traveling van along a linear path. A preliminary investigation on a cooperative SAR system aimed at increasing the resolution in scarce bandwidth conditions is by our previous work [10]. The recent work in [11] provide a comparison between compares SAR imaging and occupancy grid maps, showing the SAR superiority in terms of imaging accuracy.

All the aforementioned works underline how the knowledge about instantaneous radar position is of utmost importance for automotive SAR systems. Errors in motion estimation, due to inaccurate navigation data, make the SAR images to appear

M. Manzoni, D. Tagliaferri, M. Rizzi, Stefano Tebaldini, Andrea Virgilio Monti-Guarnieri, Claudio Maria Prati are with the Department of Electronics, Information and Bioengineering, Politecnico di Milano, Milano, MI, 20133 Italy. E-mails: {marco.manzoni,dario.tagliaferri,marco.rizzi,stefano.tebaldini, andrea.montiguarnieri,claudio.prati}@polimi.it

Monica Nicoli is with the Department of Management, Economics and Industrial Engineering, Politecnico di Milano, Milano, MI, 20133 Italy e-mail: monica.nicoli@polimi.it

Ivan Russo and Christian Mazzucco are with Huawei Technologies Italia S.r.l., Segrate, 20054 Italy. E-mail: {ivan.russo,christian.mazzucco}@huawei.com

Sergi Duque is with Huawei Technologies Duesseldorf GmbH, Munich office, 80992 Munich. E-mail: sergio.duque.biarge@huawei.com

Umberto Spagnolini is with the Department of Electronics, Information and Bioengineering, Politecnico di Milano, Milano, and Huawei Industry Chair. E-mail: umberto.spagnolini@polimi.com

rotated and defocused [12]. In principle, SAR requires navigation accuracy to be better than the wavelength (4 mm in W-band) [13], but the requirement is on the *relative* motion within the synthetic aperture, that extends up to tens of centimeters. Early works on automotive SAR [14], [15] propose simple accelerometer- and/or gyroscope-based Motion Compensation (MoCo), other [16] consider the usage of odometric wheel speed, for approximately linear trajectories. Our previous work [17] demonstrated a good SAR imaging quality in urban scenarios, employing an *ad-hoc* fusion of multiple sensors such as Global Navigation Satellite System (GNSS), Inertial Measurement Units (IMUs), odometer and steering angle. However, these former works highlighted the need of a proper residual motion correction in arbitrary dynamic conditions, where automotive-grade navigation solutions are not accurate enough.

Therefore, the residual motion estimation and compensation is still and open issue. Traditionally, air-borne and space-borne SAR systems make use of radar data on top of navigation ones to refine the positioning accuracy with an *autofocus* procedure [18]–[22]. By and large, all autofocus routines are characterized by the use of detected targets in lower resolution images to estimate the residual platform velocity, using the navigation-estimated data as *a-priori* information. On the contrary, very little work has been done in the automotive field, where simple yet effective approaches are of utmost importance. The most relevant contributions on residual motion estimation and compensation are in [23]–[27]. In [23], for instance, an autofocus procedure has been employed for the focusing of SAR images without dealing with MIMO SAR and providing just simulation results. In [24], a complete automotive-based SAR system has been proposed, based on a new approach for motion compensation. As the vehicle changes its velocity, the radar's parameters such as the pulse repetition frequency is changed, to avoid distortions in the final SAR image. The paper however does not cope with errors in the knowledge of the vehicle trajectory. Two similar approaches are in [26] and [27]. In the former, the authors use a standard range-Doppler radar to refine the ego-motion estimation of the vehicle. This information is not used, however, to focus a SAR image. In the latter, instead, two radars are used: one for the ego-motion estimation and the other for the SAR image formation.

To the best of authors' knowledge, no work discusses the theoretical and practical *requirements* of a motion compensation routine in the specific automotive context. In this paper, we analyze the effect of typical vehicle motion estimation errors on SAR imaging, highlighting the major sources of image degradation and providing the theoretical requirements in terms of maximum tolerable velocity errors. Then, we outline a possible autofocus workflow, exploiting a set of co-registered low-resolution images obtained by focusing the data received by a MIMO radar mounted on the vehicle. These low-resolution images provide the location of a set of Ground Control Points (GCPs) that are first used to retrieve the residual Doppler frequency and, consequently, the velocity error. We provide the guidelines for correctly choosing GCPs to avoid possible pitfalls that will degenerate into erroneous residual motion estimation and, consequently, to image degradation. For instance, we give insights to properly selecting the GCPs as well as the effects on SAR imaging of an error in the focusing height and wrong angular localization of a GCP. The expected theoretical performance of the residual motion estimation and compensation are also assessed. It is worth remarking that the contribution of this paper is not to propose a novel autofocus algorithm, but rather to emphasize all the possible factors affecting the motion compensation performance in typical automotive scenarios, where a real-time or quasi-real-time SAR imaging is required. Therefore, we also discuss the computational burden of autofocus, opting for simple yet effective processing options.

The work is validated by experimental data gathered by a 77 GHz MIMO radar mounted on the front bumper of a car in a frontal-looking configuration. The vehicle is purposely equipped with navigation sensors to provide the prior trajectory estimation, input of the autofocus procedure. The results confirm the proposed approach's validity, which allows obtaining cm-accurate images of urban environments.

The paper is organized as follows: in Section II, an introduction to Frequency Modulated Continuous Wave (FMCW) MIMO SAR processing is provided; Section III reports the analytical derivation of the effects of motion errors on SAR focusing and provides the theoretical limits to the accuracy of navigation data for a correct SAR imaging of the environment. Section IV describes the proposed autofocus workflow, validated with experimental data in Section V. Finally, Section VI draws the conclusion.

II. FMCW SAR PROCESSING

For the sake of clarity, in this section we propose a review of the core aspects of FMCW radars [28], MIMO and SAR processing. Each system is described, the geometry of the problem is explained, strengths and limitations are reported.

A. FMCW Preliminaries

Let us consider a FMCW radar operating in W-band, located in the origin of a 2D scenario, emitting a chirp signal of duration T_p every Pulse Repetition Interval (PRI). The emitted signal is:

$$s_{tx}(t) = \exp\{j(2\pi f_c t + \pi K t^2)\} \times \mathrm{rect}\left[\frac{t}{T_p}\right] \qquad (1)$$

where t is the *fast-time* variable, f_c is the carrier frequency, K is the chirp rate measured in [Hz/s] and the overall frequency sweep covers a bandwidth B. After range compression, the demodulated and compressed signal can be expressed as [29]:

$$s_{rc}(r; r_0) = T_p \,\mathrm{sinc}\left[\frac{r - r_0}{\rho_r}\right] \exp\left\{-j\frac{4\pi}{\lambda} r_0\right\} \qquad (2)$$

where λ is the carrier wavelength and $\rho_r = c/(2B)$ is the range resolution.

For an exemplary bandwidth $B = 3$ GHz, the range resolution is approximately 5 cm. A radar system with a single antenna will provide a resolution equal to the beam-width

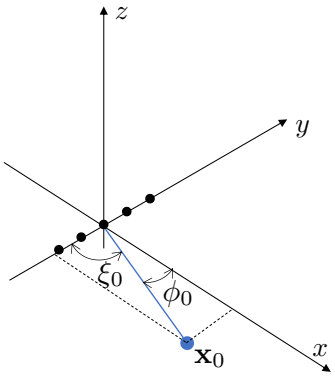

(a) MIMO

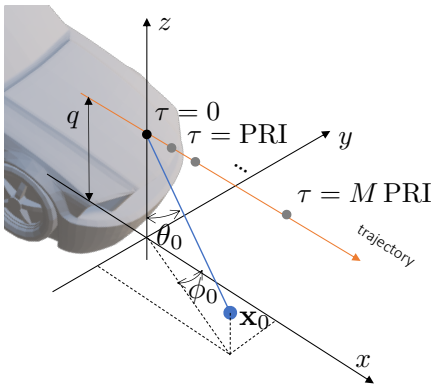

(b) SISO SAR

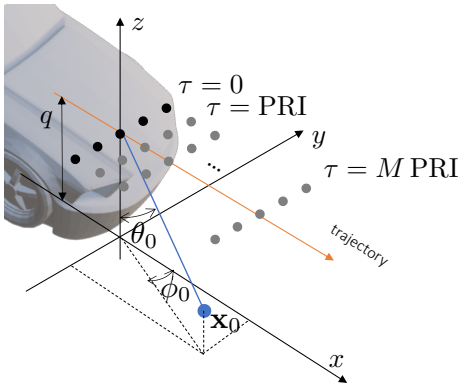

(c) MIMO SAR

Fig. 1. Geometry of the radar acquisition: (a) MIMO radar; (b) SISO SAR, at height q from ground, consisting of a single-antenna moving platform, transmitting a pulse for each PRI; (c) MIMO SAR with antenna array orthogonal to motion (forward looking configuration). Notice that other deployments of the radar are possible (for arbitrary squint angles)

in the direction orthogonal to range (azimuth). To provide an enhanced angular resolution it is common practice to use arrays of antennas, either real or virtual.

B. MIMO Processing

By using a MIMO radar, we have N_{tx} transmitting antennas and N_{rx} receiving . Each possible pair of TX-RX form a virtual radar channel leading to an equivalent virtual array composed by $N = N_{tx} \times N_{rx}$ virtual elements. Figure 1a shows a Uniform Linear Array (ULA) displaced along y, with an inter-antenna spacing of Δy.

Let us consider a 2D scenario. According to (2), the Rx signal at the n-th antenna from the target in $\mathbf{x}_0$ is:

$$s_{rc}(r, n; \mathbf{x}_0) = T_p \,\text{sinc}\left[\frac{r - r(n;\mathbf{x}_0)}{\rho_r}\right] \times \\ \times \exp\left\{-j\frac{4\pi}{\lambda} r(n;\mathbf{x}_0)\right\} \tag{3}$$

where $r(n;\mathbf{x}_0)$ is the distance from the target in $\mathbf{x}_0$ to the n-th antenna. Assuming a plane wave impinging the antenna array, it is:

$$r(n;\mathbf{x}_0) \approx r_0 - n\Delta y \sin\phi_0 \tag{4}$$

where $r_0 = r(0;\mathbf{x}_0)$ is the distance between the target and the center of the array and $\phi_0 = \tan^{-1}(y_0/x_0)$ is the observation angle (angular position of the target in the FOV). Combining (3) with (4), we obtain:

$$s_{rc}(r, n; \mathbf{x}_0) = T_p \,\text{sinc}\left[\frac{r - r_0}{\rho_r}\right] \times \\ \times \exp\left\{-j\frac{4\pi}{\lambda} r_0\right\} \exp\left\{j\frac{4\pi}{\lambda} n\Delta y \sin\phi_0\right\}, \tag{5}$$

i.e., a truncated spatial sinusoid across the array of frequency $f_x = (2/\lambda)\sin\phi_0$. The corresponding array resolution is:

$$\rho_\phi = \frac{\lambda}{2N\Delta y\,\cos\phi} \quad [\text{rad}]. \tag{6}$$

In Figure 2, we show an example from real data of a MIMO image acquired by an 8 channel array: the angular resolution is roughly 15 deg at the boresight.

C. SAR Processing

The core of SAR is to jointly process several radar pulses gathered by a radar mounted on a moving platform to improve the resolution of a MIMO radar. For the sake of simplicity, let us consider a single antenna moving on a platform and a target in $\mathbf{x}_0 = [x_0, y_0, z_0]^{\mathrm{T}}$ (3D scene). The geometry of the problem is depicted in Figure 1b. The RC signal can be written by substituting in (3) the antenna index n with the *slow-time* τ:

$$s_{rc}(r, \tau; \mathbf{x}_0) = T_p \,\text{sinc}\left[\frac{r - r(\tau,\mathbf{x}_0)}{\rho_r}\right] \times \\ \times \exp\left\{-j\frac{4\pi}{\lambda} r(\tau,\mathbf{x}_0)\right\}. \tag{7}$$

There are several algorithms that can be used for the so-called *focusing*. The most adequate for non linear trajectories is the Time Domain Back Projection (TDBP) [30], [31]. The TDBP integral for a generic pixel in the scene $\mathbf{x} = [x, y, z]^{\mathrm{T}}$ can be written as:

$$I(\mathbf{x}) = \int_{\tau\in T} s_{rc}(r(\tau,\mathbf{x}), \tau; \mathbf{x}_0) \exp\left\{+j\frac{4\pi}{\lambda} r(\tau,\mathbf{x})\right\} \mathrm{d}\tau \tag{8}$$

where $I(\mathbf{x})$ is the final SAR image, T is the considered synthetic aperture time and $r(\tau;\mathbf{x}) = \|\mathbf{x} - \mathbf{p}(\tau)\|$ is the time-varying antenna-to-pixel distance at a given time τ, function

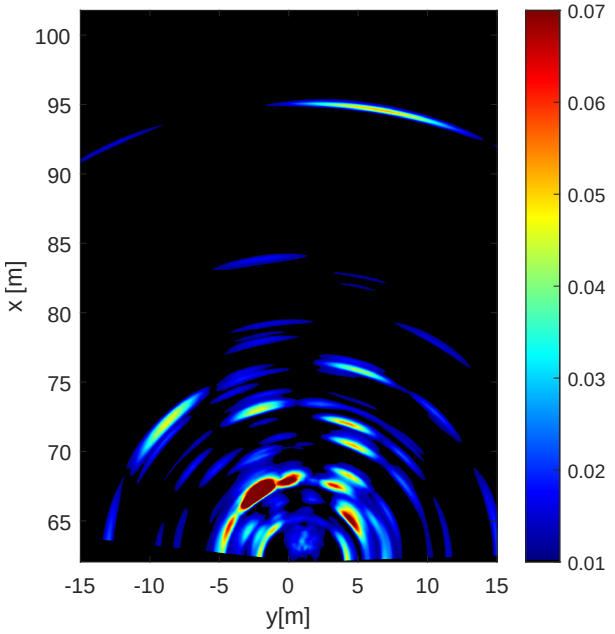

Fig. 2. MIMO image acquired by an 8 channel array. With 8 elements spaced by $\lambda/4$ the angular resolution is roughly 15 deg at the boresight.

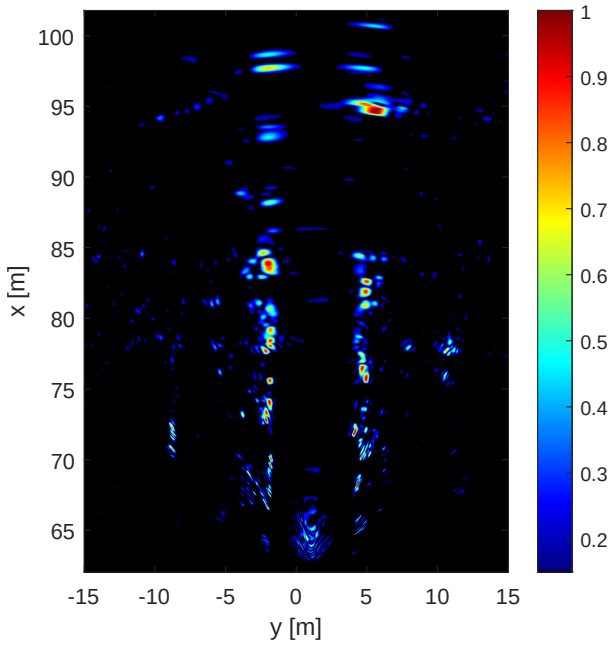

Fig. 3. MIMO SAR image focussed using an aperture length of $T = 40$ ms. The angular resolution is greatly improved with respect to the standard MIMO image. The amplitudes are normalized and in linear scale.

of the position of the Antenna Phase Center (APC) represented by the vector $\mathbf{p}(\tau) = [p_x(\tau), p_y(\tau), p_z(\tau)]^{\mathrm{T}}$.

The whole TDBP algorithm is divided in three steps: *(i)* the RC data for a single pulse is evaluated at position $r(\tau; \mathbf{x})$ *(ii)* the interpolated data is phase rotated by $\exp\{j(4\pi/\lambda)r(\tau; \mathbf{x})\}$ compensating for the two-way path phase *(iii)* the procedure is repeated for every pulse into the synthetic aperture and the results are coherently summed.

A very simple interpretation of the TDBP algorithm can be given if we assume a 2D geometry and a rectilinear trajectory of the platform with constant velocity. Although the latter assumptions may seem too simplistic for a urban environment, they are only used herein to give a intuitive interpretation of the TDBP algorithm and the aberrations induced by trajectory errors on the SAR image. However, TDBP can take into account any trajectory, possibly non-linear and with non-uniform velocity, as far as it is known during focusing.

Let us therefore assume the platform traveling at ground level (i.e, $q = 0$ or $\theta = 90$ deg for all the pixels in the FOV) along the x axis with a velocity $\mathbf{v} = [v_x, 0, 0]$. If the target is located at a generic $\mathbf{x}_0 = [x_0, y_0, 0]^{\mathrm{T}}$, we have, under plane wave approximation:

$$r(\tau; \mathbf{x}) \approx r_0 + \sin\xi v_x \tau \tag{9}$$

where $\xi = \pi/2 - \phi$.

The TDBP integral (8) now reduces to:

$$\begin{aligned} I(\mathbf{x}) &\approx \int_{\tau \in T} C \exp\left\{-j\frac{4\pi}{\lambda}[\sin\xi - \sin\xi_0]v_y\tau\right\} \mathrm{d}\tau \approx \\ &\approx T \,\mathrm{sinc}\left[\frac{2v_x T}{\lambda}(\xi - \xi_0)\right] \end{aligned} \tag{10}$$

where we assume a constant illumination of the target along the whole aperture time, i.e., $|s_{rc}(r(\tau, \mathbf{x}), \tau, \mathbf{x}_0)| = C$. The last term in (10) is valid for small angles, i.e., $\xi \to 0$ and $\xi_0 \to 0$.The expression of (10) is the Fourier transform of a truncated complex sinusoid with frequency $f_d = 2v_x\xi_0/\lambda$, therefore the result will be a cardinal sine function in the Doppler frequency domain centered in f_d.

Up to now we derived the SAR processing for a Single-Input-Single-Output (SISO) architecture. In MIMO systems, instead, we have multiple APCs (real or virtual) travelling on the same platform, as exemplified in Figure 1c for a forward looking configuration (other configurations, such as side-looking, are also possible). To have a MIMO SAR, we first observe that at each slow time τ we can form a low resolution MIMO image by simple spectral analysis (see Section II-B) or by TDBP leading to:

$$I_m(\mathbf{x}, \tau) = \sum_{n=1}^{N} s_{rc}[r(n, \tau; \mathbf{x}), n, \tau; \mathbf{x}_0] \exp\left\{j\frac{4\pi}{\lambda} r(n, \tau; \mathbf{x})\right\}, \tag{11}$$

where $I_m(\mathbf{x}, \tau)$ is the low resolution image obtained by the focusing of the N signals received at time instant τ. The final SAR image is then obtained by coherently summing all the complex-valued low-resolution MIMO images along the synthetic aperture:

$$I(\mathbf{x}) = \sum_{\tau \in T} I_m(\mathbf{x}, \tau). \tag{12}$$

The angular resolution of SAR systems improves significantly compared to conventional MIMO radars, where the effective aperture $N\Delta y$ is substituted by the synthetic aperture length $A_s = v_x\tau$:

$$\rho_{\phi}^{\mathrm{sar}} = \frac{\lambda}{2A_s \sin\phi} \quad [\mathrm{rad}] \tag{13}$$

The angular resolution is then converted into spatial resolution

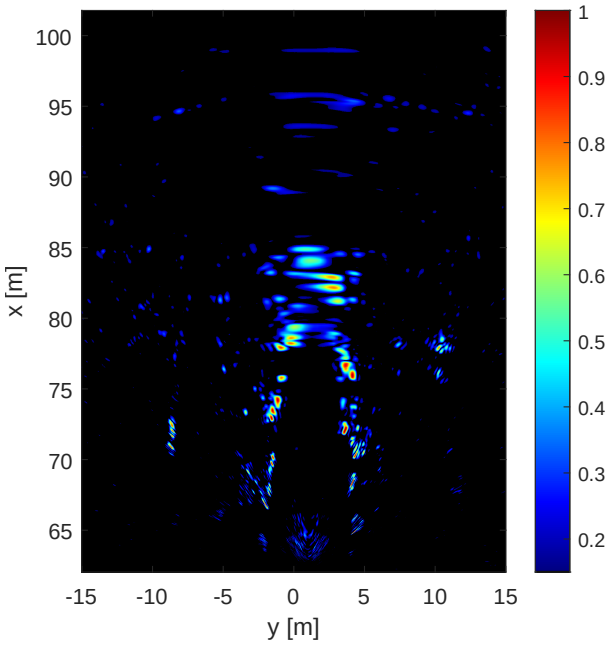

Fig. 4. The same scene of Figure 3, but now corrupted by a severe velocity error along x. The image collapses inwards. ($\Delta v_x = 35$ cm/s). The amplitudes are normalized and in linear scale.

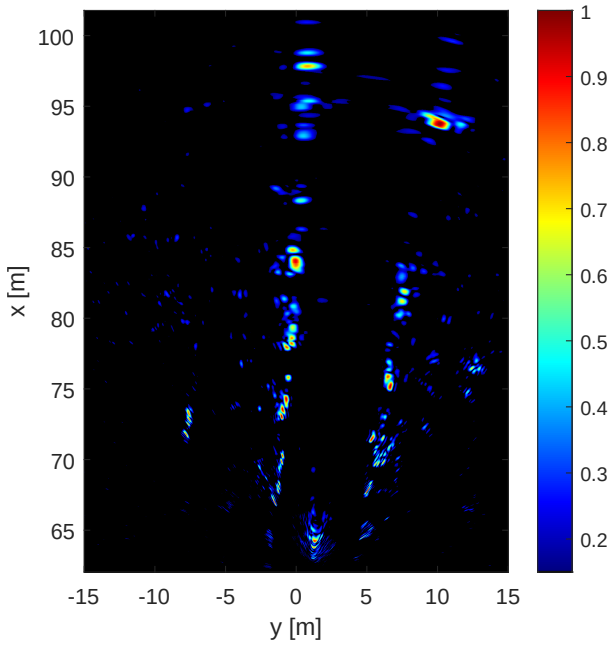

Fig. 5. The same scene of Figure 3, but now corrupted by a severe velocity error along y. The image is rotated ($\Delta v_y = 35$ cm/s). The amplitudes are normalized and in linear scale.

in the direction of motion with a linear relationship $\rho_x \approx r\rho_\phi^{\text{sar}}$. Notice that the maximum spatial resolution of a MIMO radar is for $\phi = 0$ deg, while for a SAR corresponds to $\phi = 90$ deg (orthogonal to the synthetic aperture). For a system operating at 77 GHz mounted on a vehicle traveling at 14 m/s (54 km/h), we obtain a resolution of 0.2 deg at the synthetic aperture boresight by exploiting 50 cm of aperture. The cross-range spatial resolution is 11 cm at $r = 30$ m of distance. The spatial resolution is inherently dependent on the range and angular position of the target. For example, for a target at 45 degrees w.r.t. the boresight of the array and at 20 meters of distance, the resolution obtained by exploiting 25 cm of aperture is roughly 22 cm. The same resolution is obtained exploiting the same aperture in a location at 10 meters of distance and 20 degrees of angular position. Figure 3 shows the same scene of Figure 2, but this time exploiting the car's motion to form a synthetic aperture of $T = 40$ ms. Notice that Figure 3 is a normalized SAR image (i.e., the amplitude value is between 0 and 1). The angular resolution is greatly improved allowing for better recognition and localization of the targets. The last thing to mention is the presence of moving targets in the scene. SAR imaging relies on the knowledge of the *relative* velocity between a target and the sensor. Fixing the target velocity at zero, means focusing the static scenario. In an urban environment, however, several moving targets are present. It is possible to change the scene focusing velocity leading to an image that shows just moving targets at the specific velocity. The imaging of moving targets is outside of the scope of this paper.

III. Impact of Motion Estimation Errors on SAR Focusing

We recall that each SAR processor, described by (8), requires the knowledge of the APC positions at each slow time τ for the computation of the range values $r(\tau; \mathbf{x})$. In principle, the vehicle trajectory must be known with an accuracy within the wavelength (millimeters for typical automotive radars). In practice, it is sufficient to track the *relative* APC motion along a synthetic aperture, i.e., to know the position *displacement*. In this section, we focus on velocity errors, as stationary position errors do not affect the quality of the SAR images, while linear position errors due to velocity errors lead to image distortion. We first analytically derive the effect of a velocity error on the focused SAR image $I(\mathbf{x})$, then we set the theoretical requirement on velocity estimation accuracy, discussing the implications for typical automotive SAR systems and justifying the usage of both navigation and radar data to properly perform the residual motion estimation and compensation.

In the following, we model the navigation output as a noisy biased estimate of the true vehicle's position $\mathbf{p}(\tau)$ and velocity $\mathbf{v}(\tau) = [v_x(\tau), v_y(\tau), v_z(\tau)]^{\mathrm{T}}$. Let us define the vehicle's instantaneous velocity provided by the navigation system as:

$$\mathbf{v}_{nav}(\tau) = \mathbf{v}(\tau) + \Delta\mathbf{v}(\tau), \tag{14}$$

where $\Delta\mathbf{v}(\tau) = [\Delta v_x(\tau), \Delta v_y(\tau), \Delta v_z(\tau)]^{\mathrm{T}}$ is the velocity error. In the following analytical developments, the velocity $\mathbf{v}(\tau)$ as well as the velocity estimation error $\Delta\mathbf{v}(\tau)$ from navigation data will be assumed as constant within the synthetic aperture time. We again underline that the constant velocity assumption is not mandatory for SAR imaging but greatly simplifies the problem providing a closed form solution for the effects of an error in velocity. On the other hand, the constant *velocity estimation error* from a-priori navigation

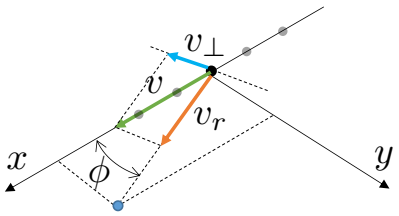

Fig. 6. Nominal velocity ($\mathbf{v}$), radial velocity v_r orthogonal velocity $v_\perp$. For the sake of simplicity we depicted the 2D geometry.

data is a reasonable assumption that allows for a simple yet realistic modeling of the signal and a robust estimation of the residual motion, as detailed in Section IV. This hypothesis has been used in several works such as [32]–[34]. A residual acceleration error, instead, has been proven in [35] to generate a slight defocusing. We deem, however, that for short apertures, in the order of tens of milliseconds, the impact of residual accelerations can be neglected (as demonstrated by Figure 15 in Section V). In any case, for longer integration times, the problem can be solved by portioning the data into sub-apertures and treat them separately by assuming no acceleration error inside each sub-aperture.

From (9), we observe that a constant velocity error maps to a linear range over time, and therefore to a linear phase. If the trajectory is perfectly known ($\Delta\mathbf{v} = \mathbf{0}$), the complex exponential in the TDBP integral of (8) will perfectly compensate the phase term of (7) on the pixel $\mathbf{x}_0$ where the target is located, leading to a constructive sum and to a well focused image. Conversely, if the estimate of the trajectory contains an error $\Delta\mathbf{v} \neq \mathbf{0}$, the phase term in (7) will not be perfectly compensated in (8), thus leading to a destructive sum and to a *defocused* image. Moreover, there is an angular displacement of the target in the SAR image leading to a wrong localization. To gain insight on the role of velocity errors in automotive SAR imaging, consider again 2D geometry, with a vehicle traveling along x at ground level ($q = 0$) at velocity v_x and a target placed in $\mathbf{x}_0 = [0, r_0, 0]^{\mathrm{T}}$. For a velocity error in the direction orthogonal to the motion ($\Delta v_y \neq 0$), the range expression (9) for small angles ξ becomes:

$$r(\tau; \mathbf{x}) \approx r_0 + \sin\xi\, v_x\tau + \cos\xi\, \Delta v_y \tau \tag{15}$$

and the TDBP integral for small angles ξ (10) can be then rewritten as:

$$I(\mathbf{x}) \approx \int_{\tau\in T} C \exp\left\{-j\frac{4\pi}{\lambda}\left(\xi - \xi_0 - \frac{\Delta v_y}{v_x}\right) v_x\tau\right\} \mathrm{d}\tau, \tag{16}$$

that is again a Fourier integral resulting in a sinc function, but now centered in $\xi_0 - (\Delta v_y / v_x)$. The error is in the angular localization of the target, $\Delta\xi = \Delta v_y / v_x$, converts into a position error:

$$\Delta x = r_0 \Delta\xi, \tag{17}$$

hindering the precise target localization especially for medium/long ranges. For instance, in Figure 4 we image the same scenario of Figure 3, but corrupted by a strong velocity error along the direction of motion $\Delta v_x = 35$ cm/s: the SAR image seems to collapse inward. A similar observation can be made for Figure 5, where the velocity error is in the direction orthogonal to the nominal motion ($\Delta v_y = 35$ cm/s). The scene is rotated as predicted by (16).

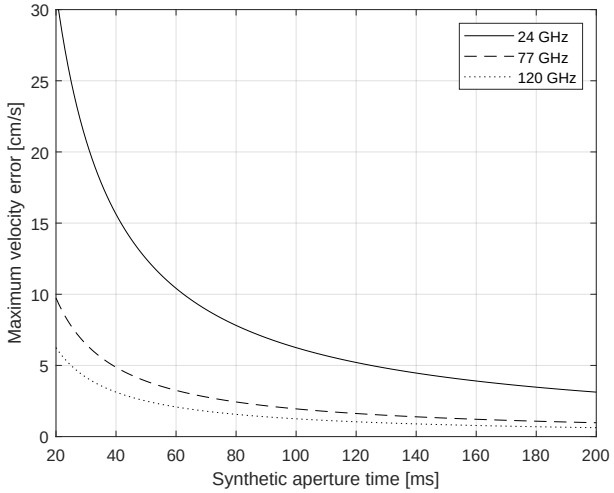

Fig. 7. The maximum tolerable velocity error in function of the total integration (aperture) time. The higher the integration time, the more stringent are the constraints on the knowledge of the car's velocity. The tolerances are evaluated for different operational frequencies of the radar.

The analysis can be generalized to the 3D domain with target position $\mathbf{x} = [x, y, z]^{\mathrm{T}}$ (at range $r = \sqrt{x^2 + y^2 + z^2}$ from the center of the synthetic aperture) and 3D velocity of the vehicle $\mathbf{v} = [v_x, v_y, v_z]^{\mathrm{T}}$. The phase of the received signal in (7) can be linearized as:

$$\psi(\mathbf{x}, \tau) \approx \frac{4\pi}{\lambda} r - \left(\mathbf{k}(\mathbf{x})^{\mathrm{T}}\mathbf{v}\right)\tau \tag{18}$$

where

$$\mathbf{k}(\mathbf{x}) = \frac{4\pi}{\lambda}[\sin\theta\cos\phi,\ \sin\theta\sin\phi,\ \cos\theta]^{\mathrm{T}}. \tag{19}$$

An error in the velocity is therefore transferred into a phase error

$$\Delta\psi^v(\mathbf{x}, \tau) = \frac{\partial\psi(\mathbf{x}, \tau)}{\partial\mathbf{v}}\Delta\mathbf{v} = \left(\mathbf{k}(\mathbf{x})^{\mathrm{T}}\Delta\mathbf{v}\right)\tau. \tag{20}$$

When $\Delta\mathbf{v} = \mathbf{0}$, the residual phase $\Delta\psi^v(\mathbf{x}, \tau)$ over a target at $\mathbf{x}$ is zero; conversely, when $\Delta\mathbf{v} \neq \mathbf{0}$, the phase shows a linear behavior with τ, representing a residual Doppler frequency. It is also interesting to notice that the phase error is higher in those areas of the FOV pointed by vector $\Delta\mathbf{v}$. If the dominant contribution of the velocity error is in the direction of motion x, for instance, the area of the final image that will be more corrupted by the velocity error is the one around x.

It is now useful to assess the maximum tolerable velocity error. From (16), a velocity estimation error maps into a target positioning error in the final SAR image as well as in a mild defocusing effect. The latter effect has less impact, as it is quantitatively discussed in Appendix. The maximum tolerable velocity error is defined as the one that induces a localization error within the angular resolution. Eq. (16) can be generalized as:

$$\frac{\Delta v_r^{\max}}{v_\perp} = \frac{\lambda}{2A_s^\perp} \tag{21}$$

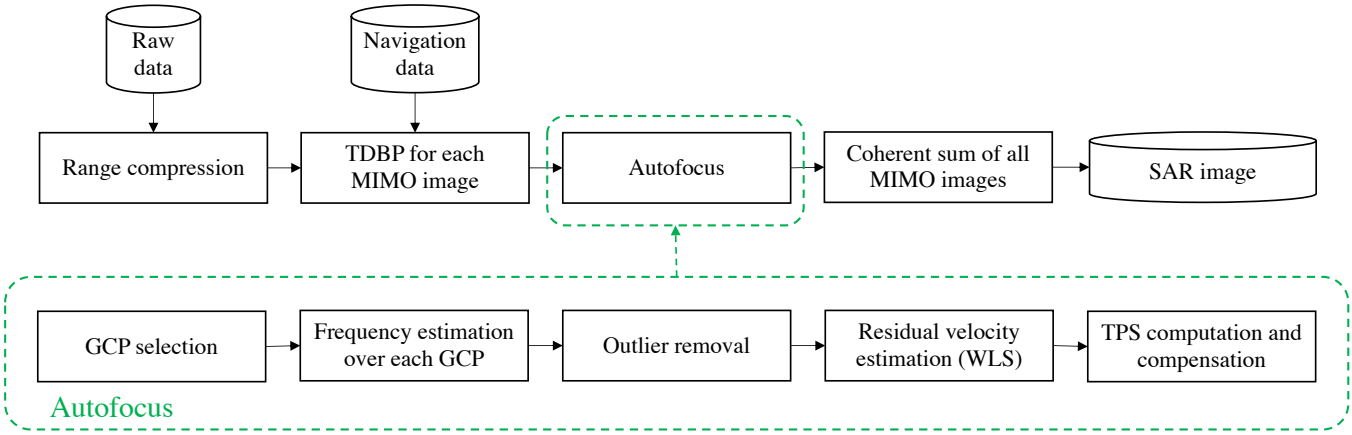

Fig. 8. Block diagram of the SAR focusing pipeline. The autofocusing procedure is a key part of the workflow.

where $\Delta v_r^{\max}$ is the maximum tolerable *radial* velocity error in an arbitrary direction defined by (θ, ϕ) (line of sight), $v_\perp$ and $A_s^\perp$ are, respectively, the nominal vehicle's velocity and the component of the synthetic aperture orthogonal to the line of sight. In Figure 6 the geometry of acquisition is depicted with the quantities just mentioned highlighted. We can also express the absolute tolerable velocity by recognizing that $A_s^\perp = v_\perp T$, where T is the integration time, thus:

$$\Delta v_r^{\max} = \frac{\lambda}{2T} \tag{22}$$

Figure 7 depicts the maximum tolerable radial velocity error as function of the total integration time and for different operational wavelengths. For a long integration time (high azimuth resolution) and shorter wavelengths, the requirements on the accuracy become very strict, in the order of 1 cm/s. For instance, for a car moving at 15 m/s, an angular resolution of $\rho_\phi^{\text{sar}} = 0.2$ deg at $\phi = 90$ deg (allowing 1 m of cross-range resolution at 30 m at 77 GHz) implies $T \approx 40$ ms, therefore the velocity error shall be within $v_r^{\max} = 5$ cm/s. Notice that, reducing the frequency of operation, e.g., to 24 GHz, does not relax the requirement: an angular resolution of $\rho_\phi^{\text{sar}} = 0.2$ deg requires an aperture time $T \approx 125$ ms, leading again to $\Delta v_r^{\max} \approx 5$ cm/s. Automotive-legacy navigation systems can provide an average velocity error ranging from 5 cm/s down to $2-3$ cm/s for expensive commercial Real-Time Kinematic (RTK) setups, possibly integrating GNSS, inertial sensors and magnetometers [36]. However, these systems heavily rely on GNSS signals, that may be absent or inaccurate in some scenarios (urban canyons with strong multipath or tunnels). Moreover, car navigation systems must deal with unpredictable driver's maneuverings, leading to a velocity error that could be as high as $10-20$ cm/s [37]. Although the fusion of inexpensive heterogeneous in-car sensors data was demonstrated to provide accurate imaging in moderate dynamics [17], a reliable SAR imaging for autonomous driving applications calls for the integration of navigation *and* radar data.

IV. Motion error estimation and compensation

This section outlines the proposed residual motion estimation and compensation technique to estimate and compensate trajectory errors starting from a set of low resolution MIMO images $\{I_m(\mathbf{x}, \tau)\}_{\tau \in T}$. We remark that this paper aims at providing the practical guidelines for the implementation of autofocus in the automotive scenario and discuss possible pitfalls, rather than proposing novel autofocus kernels, as the core is well known in the literature [33]. After the estimation of the motion error, each MIMO image is first corrected by a phase term referred to as Trajectory Phase Screen (TPS), then a well-focused SAR image is obtained by (12). Figure 8 shows the complete SAR data processing and autofocus workflow. In the following, we detail each portion of the block diagram.

A. From raw data to a stack of low-resolution images

The vehicle is equipped with a MIMO FMCW array able to generate an equivalent virtual array of N elements. At each slow time, each one of the N elements of the array receives a radar echo. Each received signal is first RC and then subject to the TDBP for the generation of the M low resolution images in the duration of the synthetic aperture T: each image $I_m(\mathbf{x}, \tau)$ is formed by back-projecting in the FOV the N signals received at each APC of the array at the time instant τ. Notice that the combination of PRI and number of MIMO channels of the radar must ensure to have unambiguous low resolution images. If the TDBP is performed over a common grid for all the slow time instants, all the images are already compensated for range migration. Conversely, if the focusing of the MIMO images is done using a simple Fourier transform as discussed in Section II-B, the images must be then co-registered to a common grid through an interpolation step [30]. The former approach has been used in this work.

B. Autofocus

The core of the procedure, i.e., the autofocus routine, takes as input the set of M low resolution images $\{I_m(\tau, \mathbf{x})\}_{\tau \in T}$. As discussed in Section III, the presence of a constant error in the estimated velocity $\Delta \mathbf{v}$ by navigation leads to a linear residual range (or phase) after TDBP, leading to a distorted image. The autofocus procedure starts from the linear residual

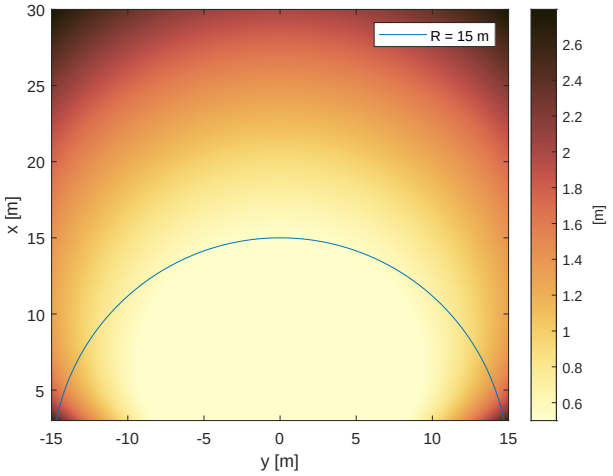

Fig. 9. Maximum tolerable focusing height error on GCP. The nominal vehicle velocity is set to 15 m/s along x, the nominal radar height over ground is 0.5 m, the maximum radar slant range is 30 m. Notice that in far range, the system becomes tolerable to focusing heights errors.

phase $\Delta\psi^v(\mathbf{x},\tau)$ in (20), representing a complex sinusoid of angular frequency:

$$\Delta\omega(\mathbf{x}) = \mathbf{k}(\mathbf{x})^{\mathrm{T}}\Delta\mathbf{v}, \tag{23}$$

that provides a single equation for three unknowns (the three components of the velocity error). Exploiting the low-resolution images at each slow time, it is sufficient to detect few stable GCPs in the scene to have an overdetermined linear system of equations. If we consider a total of P stationary GCPs we can write:

$$\underbrace{\begin{bmatrix}\Delta\omega(\mathbf{x}_0)\\ \Delta\omega(\mathbf{x}_1)\\ \Delta\omega(\mathbf{x}_2)\\ \vdots\\ \Delta\omega(\mathbf{x}_P)\end{bmatrix}}_{\Delta\boldsymbol{\omega}} = \underbrace{\begin{bmatrix}k_x^0 & k_y^0 & k_z^0\\ k_x^1 & k_y^1 & k_z^1\\ k_x^2 & k_y^2 & k_z^2\\ \vdots & \vdots & \vdots\\ k_x^P & k_y^P & k_z^P\end{bmatrix}}_{\mathbf{K}} \underbrace{\begin{bmatrix}\Delta v_x\\ \Delta v_y\\ \Delta v_z\end{bmatrix}}_{\Delta\mathbf{v}} + \underbrace{\begin{bmatrix}n_0\\ n_1\\ n_2\\ \vdots\\ n_P\end{bmatrix}}_{\mathbf{n}} \tag{24}$$

where $\mathbf{n} \sim \mathcal{CN}(\mathbf{0}, \sigma_n^2\mathbf{I})$ is the circularly complex Gaussian noise vector of power σ_n^2 representing the uncorrelated noise on the estimates of the residual frequencies $\Delta\boldsymbol{\omega}$. The process of selection of stable GCPs can be performed by looking at the amplitude statistics of the scene. In particular, we opt for the computation of the *incoherent* average (i.e., the average of the amplitudes) of all the M low resolution images and take just the brightest targets. Since the linear system (24) has only three unknowns, it is typically sufficient to detect 20 to 50 GCPs to obtain a reliable estimate. Therefore, the thresholding on the amplitude for the GCP selection can be very stringent. The rejection of moving targets will be discussed later on in this section. Another key aspect in the selection of GCP is the accuracy on their localization. An error in the focusing height and/or an error in the estimation of the angular position of the GCPs can prevent a correct estimation of the residual motion error.

1) Error in the focusing height of GCP: In (8), the 3D coordinate $\mathbf{x}$ of every pixel of the backprojection grid can be arbitrarily chosen. It is common practice to choose a fixed focusing height, i.e., $\mathbf{x} = [x, y, z = z']^{\mathrm{T}}$. In a real scenario, however, the height of the target is not known and it is possibly different from z' [38]. The difference between the true position and the focusing plane is denoted by Δz. If the target is not truly at that position, another linear residual phase term arises. The expression of such residual phase can be easily derived considering that an error on z is equivalent to an error on the elevation angle θ, thus:

$$\Delta\psi^z(\mathbf{x},\tau) = \frac{\partial\psi(\mathbf{x},\tau)}{\partial\theta}\Delta\theta = \left[\left(\mathbf{k}'_\theta(\mathbf{x})^{\mathrm{T}}\mathbf{v}\right)\Delta\theta\right]\tau \tag{25}$$

where $\mathbf{k}'_\theta(\mathbf{x}) = (4\pi/\lambda)[\cos\theta\cos\phi,\ \cos\theta\sin\phi,\ -\sin\theta]^{\mathrm{T}}$ is the derivative of $\mathbf{k}(\mathbf{x})$ with respect to θ and

$$\Delta\theta = \frac{\Delta z}{r\sin\theta}. \tag{26}$$

Notice that (25) is again linear in slow time: both an error in the velocity and an error in the focusing height manifest as a linear phase in time. The residual linear phase over a GCP depends on the nominal velocity of the vehicle $\mathbf{v}$, the angles (θ, ϕ), the range r and the error of focusing height Δz. It is now possible to compute the maximum tolerable error in term of Δz which will again depend on the GCP position (r, θ, ϕ) and on the vehicle velocity $\mathbf{v}$. Exploiting the requirement on the radial velocity (22), the maximum tolerable height error is the one that generates a Doppler frequency corresponding to $\Delta v_r^{\max}$. In Figure 9, we show the maximum tolerable height error for 77 GHz radar with $T = 200$ ms integration time, represented for each pixel in the scene. Notice that, according to (26), in far range the system is very robust even to big elevation errors. This is a direct consequence of large r and steep incidence angles ($\theta \approx 90$ deg). The suggestion is then to select GCPs in the far range of the scene. In any case, the residual linear phase due to target's elevation can be also estimated and compensated by an interferometric processing, disposing of at least two ULAs displaced along z.

2) Error in the angular localization of GCP: The same reasoning used for an error in the focusing height can be applied to an error in the angular localization of a GCP. Without velocity focusing height errors, the residual Doppler frequency is exactly zero over a given target. Due to the finite sampling of the MIMO images, however, it can happen that the peak of the Impulse Response Function (IRF) representing the target is not detected, as shown in Figure 10. The mis-detection could happen also due to the in-avoidable presence of noise. In blue, the continuous IRF with an angular resolution given by the physical length of the array, the sampling positions being depicted in red while the detected GCP in purple. If the detected GCP is not at the peak of the cardinal sine function, a residual Doppler frequency is present.

Let us call $\Delta\phi$ the error on the angular localization of a GCP. We have:

$$\Delta\psi^\phi(\mathbf{x},\tau) = \frac{\partial\psi(\mathbf{x},\tau)}{\partial\phi}\Delta\phi = \left[\left(\mathbf{k}'_\phi(\mathbf{x})^{\mathrm{T}}\mathbf{v}\right)\Delta\phi\right]\tau \tag{27}$$

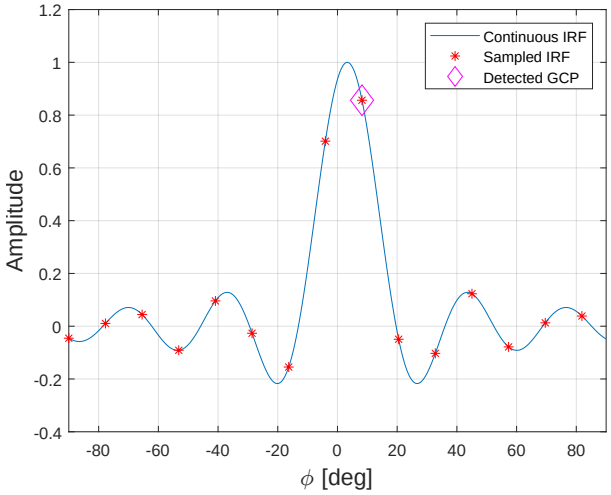

Fig. 10. Example of angular detection error on a GCP: (blue) the continuous impulse response function of the MIMO array, (red) Sampling position, (purple) the detected GCP is not exactly on the peak of the cardinal sine function.

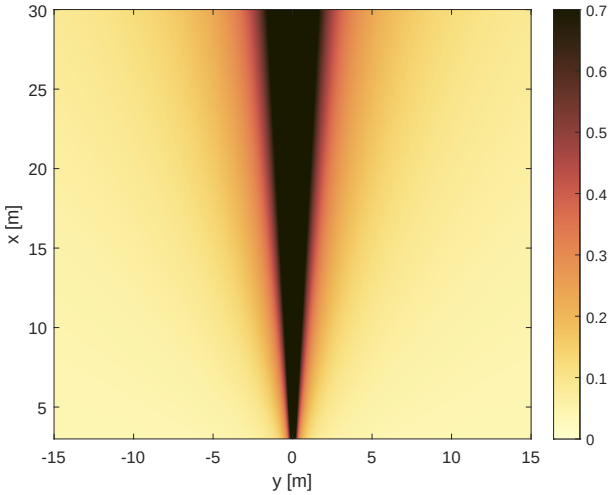

Fig. 11. Maximum tolerable angular error in GCP detection. The nominal vehicle velocity is set to 15 m/s along x, the nominal radar height over ground is 0.5 m, the maximum radar slant range is 30 m. The system is tolerable to angular errors in the direction of the motion.

where $\mathbf{k}'_\phi(\mathbf{x}) = (4\pi/\lambda)[-\sin\theta\sin\phi,\ \sin\theta\cos\phi,\ 0]^{\mathrm{T}}$ is the derivative of $\mathbf{k}(\mathbf{x})$ with respect to ϕ. The residual angular Doppler frequency is then:

$$\Delta\omega^{\phi} = \frac{\partial\psi(\mathbf{x},\tau)}{\partial\phi}\Delta\phi = \left(\mathbf{k}'_\phi(\mathbf{x})^{\mathrm{T}}\mathbf{v}\right)\Delta\phi = \frac{4\pi}{\lambda}v_\perp\Delta\phi. \quad (28)$$

Again, the maximum tolerable angular error is the one that will generate a Doppler frequency corresponding to $\Delta v_r^{\max}$. In Figure 11, the maximum tolerable angular error $\Delta\phi$ is depicted for every pixel in the field of view. The car is supposed to travel along x at 15 m/s. In this case, $v_\perp$ is ≈ 0 for the pixels exactly in front of the car, thus allows for a larger $\Delta\phi$. The worst case is for $\phi \approx 90$ deg, where the accuracy in GCP detection must be the maximum. GCP detection accuracy can be refined with a parabolic interpolation to reduce unwanted phase effects.
It is important to highlight that, with a sufficient number of GCPs, the angular error becomes irrelevant since the errors will be both positive and negative and the average will approach zero. The same is not true for elevation error where a significant bias towards positive or negative errors may be present.

Once the GCPs have been detected, a frequency estimation is performed through a Fast Fourier Transform (FFT) of the phase of each GCP, and the position of the peak in the frequency domain is extracted to form $\Delta\boldsymbol{\omega}$ in (24). It is possible that a moving target (bike, another vehicle, pedestrian, etc.) is detected as a GCP, preventing a correct residual motion estimation. It is mandatory to discard outliers before the inversion of (24), by imposing a threshold on the maximum frequency that is possible to find on a given GCP. As a rule of thumb, the value of the threshold can be derived from the accuracy of the navigation data: if the the nominal accuracy is, for instance, 20 cm/s, it is unlikely to find a GCP with a residual Doppler frequency much higher than the one corresponding to 20 cm/s. It is worth to stress that, the more accurate the navigation data, the more robust is the outlier rejection and, consequently, the better the performance of the whole procedure. Notice that it is of utmost importance to discard moving targets from the set of selected GCPs, otherwise performance penalties occur. The hard thresholding on the maximum allowed residual Doppler frequency allows for an easy and fast rejection of moving targets.

The linear system (24) can therefore be solved using the Weighted Least Square (WLS) method:

$$\widehat{\Delta\mathbf{v}} = (\mathbf{K}^{\mathrm{T}}\mathbf{W}\mathbf{K})^{-1}\mathbf{K}^{\mathrm{T}}\mathbf{W}\Delta\boldsymbol{\omega} \quad (29)$$

where $\mathbf{W}$ is a proper weighting matrix. Each GCP can be weighted according to some specific figure of merit such as the amplitude of the GCP or the prominence of the peak in the frequency domain. In the first case, stronger targets (higher radar cross section) will weigh more in the linear inversion while, in the latter case, more weight is given to those targets with a more pronounced linear phase behavior. We used a simple weighted linear inversion due to its low computational burden, ideal for real time applications. It is worth remarking that the matrix inversion (29) might be unstable. In a typical automotive environment, the radar is mounted close to the road, thus $\theta \approx 90$ deg for every GCP. The direct consequence is that the residual radial velocity vector of any given GCP has components only in the x, y plane and not in the z direction, therefore a residual velocity along z has no possibility to be detected with satisfactory accuracy. It is even more straightforward from (18): if $\Delta v_z \neq 0$ there is no consequence on the residual phase if $\theta = 90$ deg. The solution can be to avoid the estimation of Δv_z by removing the last column of $\mathbf{K}$ and the last row of $\Delta\mathbf{v}$. The quality of the velocity estimate $\widehat{\Delta\mathbf{v}}$ can be assessed by its covariance matrix, that is:

$$\mathbf{C}_{\widehat{\Delta\mathbf{v}}} = (\mathbf{K}^{\mathrm{T}}\mathbf{W}\mathbf{K})^{-1}\sigma_n^2. \quad (30)$$

Notice that, in practice, the exact value of σ_n^2 is unknown, but with a sufficient number of GCP it can be roughly estimated

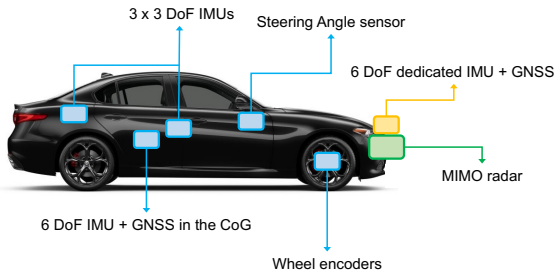

Fig. 12. Vehicle navigation equipment

TABLE I
SYSTEM PARAMETERS USED IN THE CAMPAIGN

Parameter	Value
Carrier frequency (f_c)	77 GHz
Bandwidth (B)	1 GHz
Pulse length (T_p)	55 μs
PRF	7 KHz
Active TX channels	2
Active RX channels	4
Maximum range	40 m
Geometry (Mode)	forward looking

from the residual of (24), providing some realistic values for the accuracy of the velocities' estimates. Equation (30) can provide also some insights on how to choose GCP in the scene. For the sake of simplicity, we assume equal unitary weights for each GCP ($\mathbf{W} = \mathbf{I}$), we normalize the noise power ($\sigma_n^2 = 1$) and we consider a 2D geometry ($\theta = 90$ deg). In this scenario we have:

$$\mathbf{C}_{\widehat{\Delta \mathbf{v}}} = \frac{1}{|\mathbf{K}^{\mathrm{T}}\mathbf{K}|} \begin{bmatrix} \mathbf{k}_y^{\mathrm{T}}\mathbf{k}_y & -\mathbf{k}_x^{\mathrm{T}}\mathbf{k}_y \\ -\mathbf{k}_y^{\mathrm{T}}\mathbf{k}_x & \mathbf{k}_x^{\mathrm{T}}\mathbf{k}_x \end{bmatrix} \tag{31}$$

where $\mathbf{k}_x = [k_x^0, k_x^1, \ldots, k_x^P]^{\mathrm{T}}$, $\mathbf{k}_y = [k_y^0, k_y^1, \ldots, k_y^P]^{\mathrm{T}}$, and $|\cdot|$ denotes the determinant of a matrix. If we choose all the GCPs closely spaced in front of the car (i.e., $\phi \to 0$ deg), the estimation of Δv_y will be much more unreliable than the estimate of Δv_x since $\mathbf{k}_x^{\mathrm{T}}\mathbf{k}_x \gg \mathbf{k}_y^{\mathrm{T}}\mathbf{k}_y$. The same reasoning is valid for GCPs closely spaced at the side of the car (i.e., $\phi \to 90$ deg): the only reliable estimate is on Δv_y. The extreme case is when all the GCP are closely grouped together: in this case the matrix $\mathbf{K}$ is close to be singular and the estimates of the residual velocities are useless. Notice that the residual velocities estimated in (29) can be also used to improve the ego-motion estimation of the vehicle. In this case it is sufficient to integrate the residual velocities to obtain the residual trajectory and then compensate the error in the original trajectory provided by the navigation unit.

A final note shall be made about the computational complexity of the autofocus algorithm. The workflow has been designed tailoring real-time automotive imaging for safety-critical applications, thus the computational complexity shall be very low for each step. The most demanding task is the computation of the FFT over each GCP. The computational complexity depends on the number of frequency points over which the FFT is evaluated. Nevertheless, the number of GCPs is very low (less than 50 for a reliable estimate of just two parameters). Moreover, the hard thresholdings for the selection of GCPs and outliers' rejection have a computational complexity which is negligible compared to the more demanding TDBP. The computational burden of the whole procedure is so low to allow for real-time imaging even without software/hardware optimizations.

C. SAR image formation

Once the residual velocities have been found, it is possible to compute the forward problem for each pixel $\mathbf{x}$ in the scene and for each τ (i.e., each one of the M low resolution MIMO images). This leads to a set of estimated TPS:

$$\widehat{\Delta\psi}(\mathbf{x}, \tau) = \left(\mathbf{k}(\mathbf{x})^{\mathrm{T}}\widehat{\Delta \mathbf{v}}\right)\tau \tag{32}$$

Each low resolution image is phase-compensated using the estimated TPS:

$$\widehat{I}_m(\mathbf{x}, \tau) = I_m(\mathbf{x}, \tau)\exp\left\{-j\widehat{\Delta\psi}(\mathbf{x}, \tau)\right\}. \tag{33}$$

and then coherently summed to obtain the final high-resolution SAR image

$$I(\mathbf{x}) = \sum_{\tau \in T} \widehat{I}_m(\mathbf{x}, \tau). \tag{34}$$

The final SAR image is now properly focused, localized and ready to be used in safety critical systems such as advanced autonomous driving systems.

V. RESULTS WITH REAL DATA

To validate the proposed technique, we carried out an extensive acquisition campaign using a fully equipped vehicle. The radar system is a proprietary ScanBrick® by Aresys® and it is based on the Texas Instruments AWR1243 Single-Chip 77- and 79-GHz FMCW transceiver [39]. The maximum available bandwidth is 4 GHz for a range resolution up to 3.75 cm. The mounting position of the radar on the vehicle is precisely known. The entire radar equipment is based on standard automotive hardware suitable for future mass-market production. The radar is mounted in a forward looking geometry, thus the boresight of the MIMO array is pointing in the direction of motion. We employed just 2 out of 3 Tx antennas and all the 4 Rx ones, leading to a virtual array of $N = 8$ elements, spaced by $\lambda/4$. The angular resolution of the low-resolution images $I_m(\tau; \mathbf{x})$ is approximately 16 deg.The transmitted signal has 1 GHz of bandwidth leading to a range resolution of 15 cm. We remark that the SAR angular resolution, even in forward-looking geometry, is still defined by Eq. 13. All the system's parameters are summarized in Table I. Notice that in all the previous works in literature, the radar was mounted side looking. In fact, a SAR in forward looking geometry, without an array displaced along the direction orthogonal to the motion (y) would lead to a totally left/right ambiguous SAR image. The presence of a ULA with the elements displaced along y helps to unambiguously reconstruct the image (as in our case study). The car equipment (Figure 12) is complemented by navigation sensors to provide the estimated trajectory as

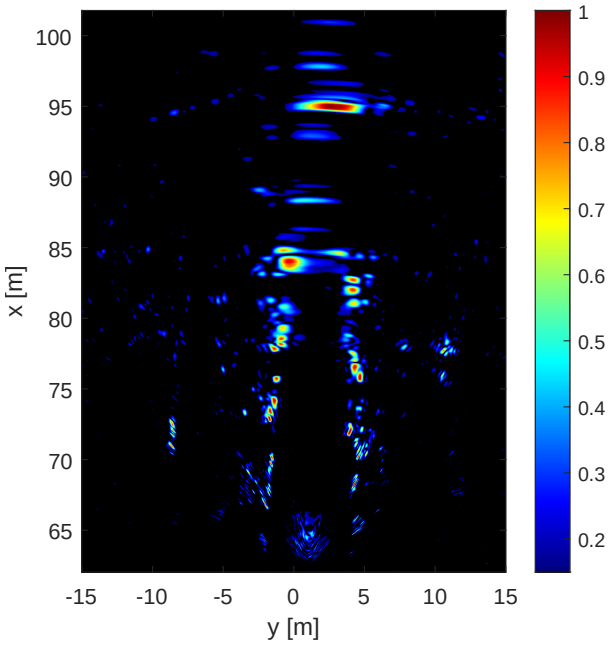

Fig. 13. SAR intensity image without employing any autofocus procedure. The amplitudes are normalized and in linear scale.

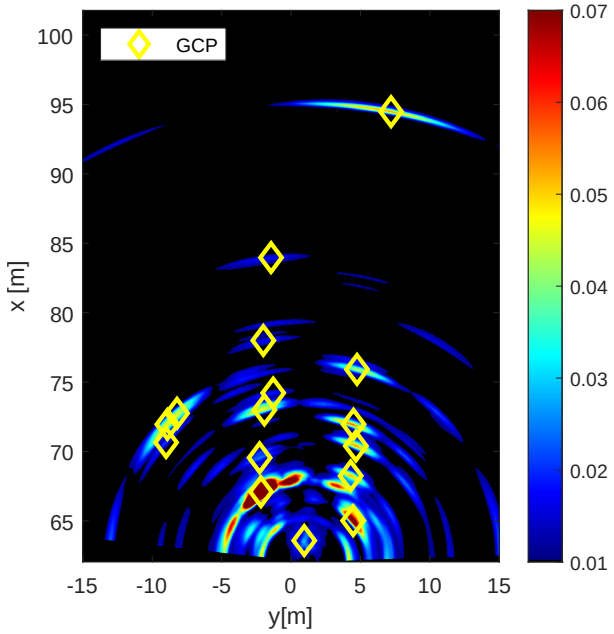

Fig. 14. Incoherent average of all the low resolution MIMO images. The selected GCPs are depicted with yellow diamonds.

input to the procedure. The on-board navigation equipment comprises: *(i)* two internal 3 Degrees of Freedom (DoF) IMUs, measuring lateral and longitudinal acceleration, along with heading rate; *(ii)* an occupant restraint controller, consisting in a 3 DoF IMU placed in the rear part of the car, measuring longitudinal and lateral acceleration as well as heading rate, the purpose is the airbag activation during a crash; *(iii)* four wheel encoders, measuring the odometric velocity of each wheel; *(iv)* a steering angle sensor at the frontal wheels; *(v)* an on-radar IMU+GNSS sensor [36]. The sensors' data are fused with an Unscented Kalman Filter (UKF) approach described in our previous work [17].

The acquisition campaign has been carried out in a straight road with several targets in the FOV of the radar. We selected a portion of the trajectory made by $M = 256$ slow time samples and we processed the dataset with and without running the autofocus workflow. The nominal speed of the vehicle in the selected synthetic aperture was 36 km/h, thus, for a PRI of 0.14 ms, leads to an average synthetic aperture length $A_s \approx 40$ cm.

The result of the SAR processing without autofocus (only navigation-based MoCo) is depicted in Figure 13. It is interesting to notice how the image is completely corrupted by an error on the estimated trajectory. The image seems to collapse inward (i.e., towards the line at $x = 0$). Some details are still preserved, nevertheless, the localization accuracy of the targets might not be sufficient for safety-critical autonomous driving systems.

The autofocus workflow starts from the detection of a set of GCPs from the incoherent average of all the low resolution MIMO images. In Figure 14, the incoherent average is represented along with the detected GCPs (highlighted in yellow). The first observation is that, as expected, the spatial resolution of the MIMO image formed with the ULA is greatly lower than Figure 13). The second and most important observation is that the low-resolution images are not severely corrupted by trajectory estimation errors as the SAR one.Over the detected GCPs, the residual Doppler frequency is then estimated through FFT. In Figure 15a, the unwrapped residual phase over all the GCPs is depicted. The phase is linear for every GCP and the slope is proportional to the residual radial velocity of the car as seen by the position of the GCP, confirming that the constant velocity estimation error is a reasonable assumption. The result of the FFT is depicted in Figure 15b and the red asterisks are the detected frequency peaks. The position of such peaks will form the observation vector $\Delta\boldsymbol{\omega}$ in (24). The frequency resolution depends on the observation time T. A trade off is now evident: longer synthetic apertures allows for higher spatial resolution and, from the autofocus perspective, a higher residual Doppler resolution. The price to be paid is the possibility of non-constant velocity errors in longer apertures (acceleration errors) and increased computational burden. It is also important to notice that Figure 15b shows the *sampled* version of the Doppler spectrum of a GCP. The sampling in the frequency domain can be made finer by zero-padding the time domain signal before the FFT. This guarantees that the position of the peak of the sinc function is precisely detected.

The inverse problem (29) is solved for the detected GCPs leading to the residual velocities in Table II, reported with the theoretical accuracy. First of all, the estimated residual velocities are within the confidence bound of the employed navigation sensors [17]. The error is higher in the direction of motion, and, since we work in a forward looking geometry, all the GCPs are distributed in front of the car, thus higher accuracy in the residual motion estimation is expected in this direction. On the other hand, the error in the direction orthogonal to the motion is much lower and estimated with more uncertainty.

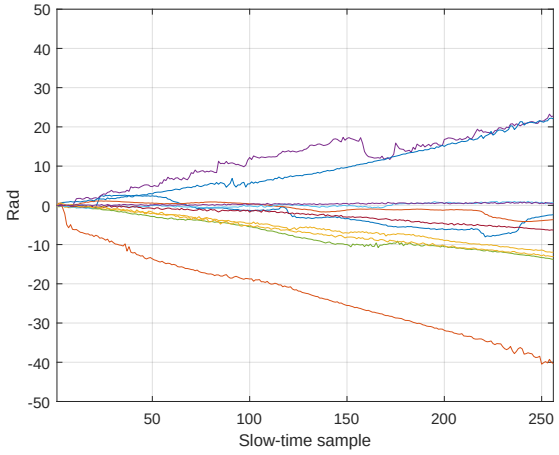

(a)

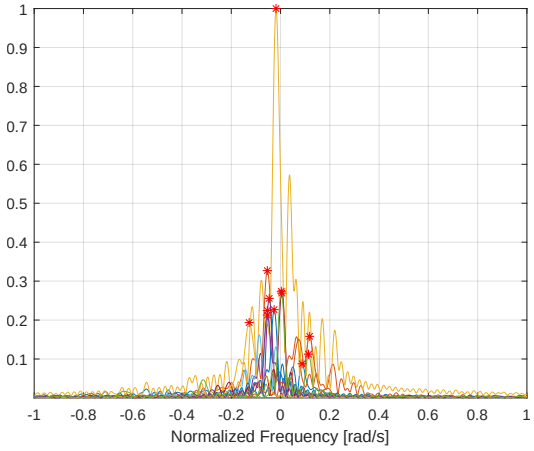

(b)

Fig. 15. (15a) Unwrapped phase over the selected GCP: a residual phase is linear in slow time indicating the presence of a residual motion error; (15b) Result of the frequency estimation over the selected GCP: a linear phase represents a sinusoid. Notice how the cardinal sines functions are not centered in zero.

Once the residual velocities are estimated, each low resolution image is TPS-compensated and the coherent average forms the final SAR image as from (34). The image is represented in Figure 16. While Figure 13 reports a collapsed scene towards the center of the image, now the profile given by the parked cars is correctly straight also in far range. A few details of Figure 16 are depicted in Figure 17. At the top of the figure we reported the image from the camera. In the lower part, three details are shown on the SAR image. The green box includes two parked cars, the yellow box shows parked cars with a free parking slot. Notice that this area was totally corrupted by the motion error in Figure 13. Lastly, the red box shows the most important detail of the experimental activity, i.e., a standing pedestrian nearby the parked car. This is a possibly dangerous scenario for autonomous driving, as a stationary pedestrian is a comparably weak target with respect to the car (in terms of radar cross section), that cannot be distinguished by the Doppler signature. However, the pedestrian is clearly separated from the car in the final image, showing the full potential of SAR imaging in automotive scenarios.

A further experimental case study is reported in Figure 18. Again, the SAR image without autofocus is corrupted by a severe residual velocity estimation error, being collapsed outward. With autofocus, the correct environment is precisely imaged (Figure 19). Some meaningful details are shown in Figure 20. At the top, the camera image showing the richness of the scene: cars, parking slots, poles, fences and buildings are present. In the green box, two cars are depicted with a free parking space in the middle. In the yellow box, we show the fence and some cars in far range, while, in the red box, parked cars at the right of the vehicle are shown.

These SAR images can now be used as an input product along with LiDAR or cameras in advanced autonomous driving systems, possibly using statistical analysis tools [40], [41].

TABLE II
RESIDUAL VELOCITY ESTIMATED BY AUTOFOCUS AND RELATED ACCURACY

Parameter	Estimate (cm/s)	Accuracy (cm/s)
Δv_x	-6.24	1.08
Δv_y	-3.64	3.06

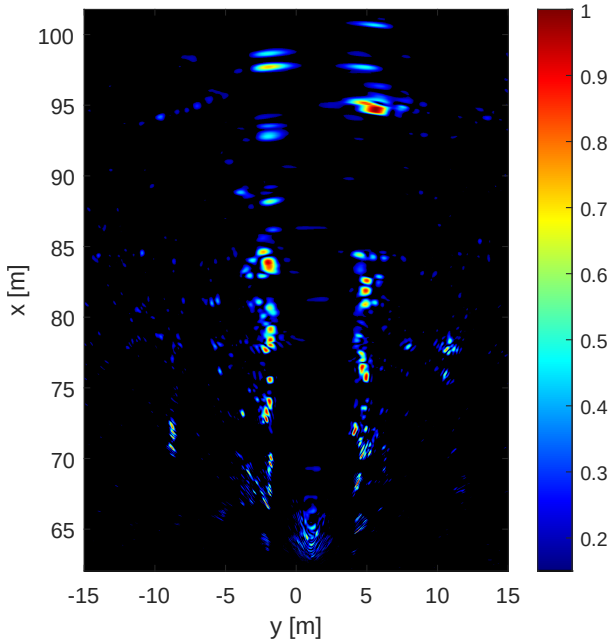

Fig. 16. Normalized SAR image after employing the proposed autofocus procedure. The amplitudes are normalized and in linear scale.

VI. CONCLUSION

The generation of SAR images requires a precise knowledge of the trajectory of the moving platform. For automotive applications and synthetic apertures of tens of centimeters to few meters length, velocity estimation errors from inaccurate navigation data are the major source of SAR image quality degradation, causing defocusing and targets' mis-localization. The higher the carrier frequency and the synthetic aperture length, the higher the accuracy needed on velocity estimation, with maximum tolerable errors as low as 1 cm/s. In these cases, inexpensive automotive-legacy navigation systems

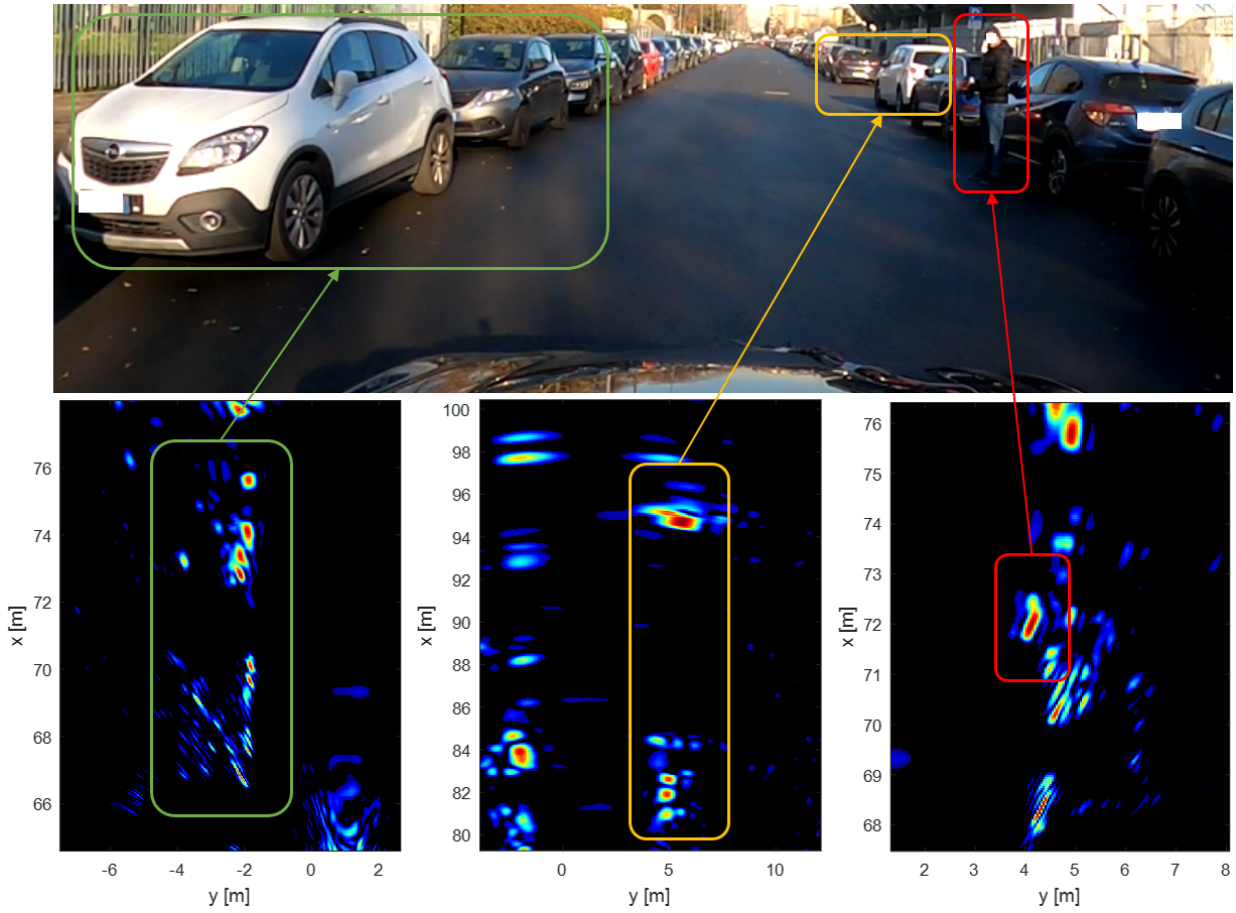

Fig. 17. (top) Optical image of the scene. (bottom left) Cars parked to the left of the moving vehicle. (bottom center) Parked car in the far field and free parking lot. (bottom right) Pedestrian standing near to a parked car. The amplitude is normalized.

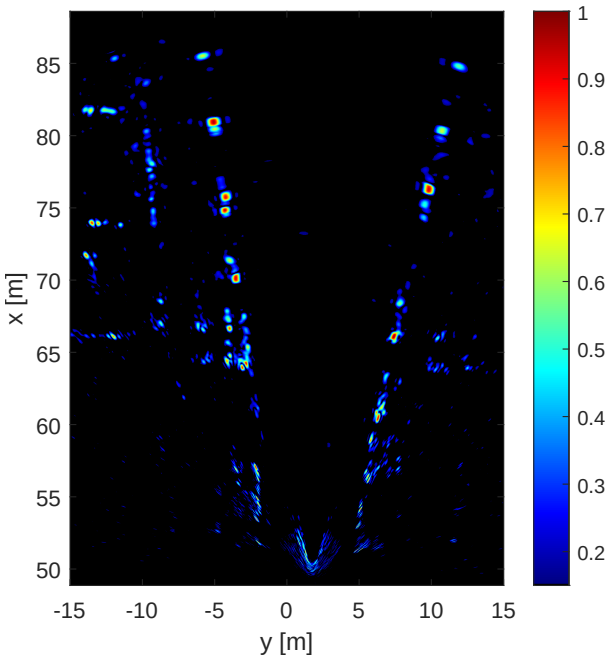

Fig. 18. Normalized SAR image before employing the proposed autofocus procedure. The amplitudes are normalized and in linear scale.

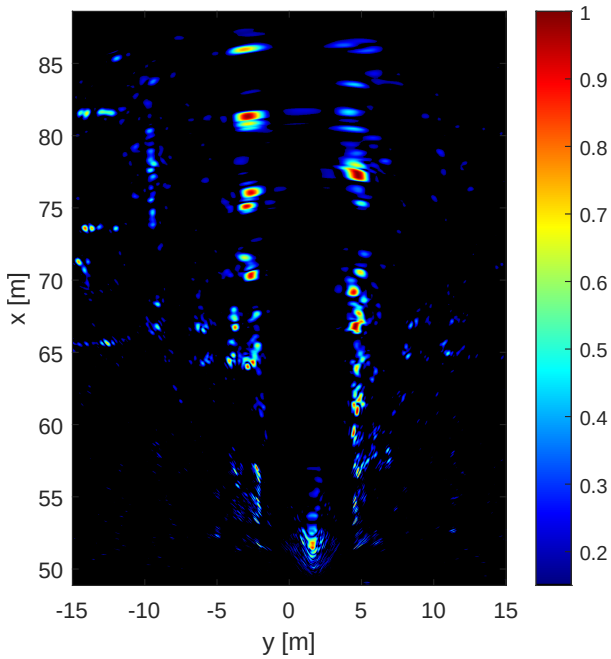

Fig. 19. Normalized SAR image after employing the proposed autofocus procedure. The amplitudes are normalized and in linear scale.

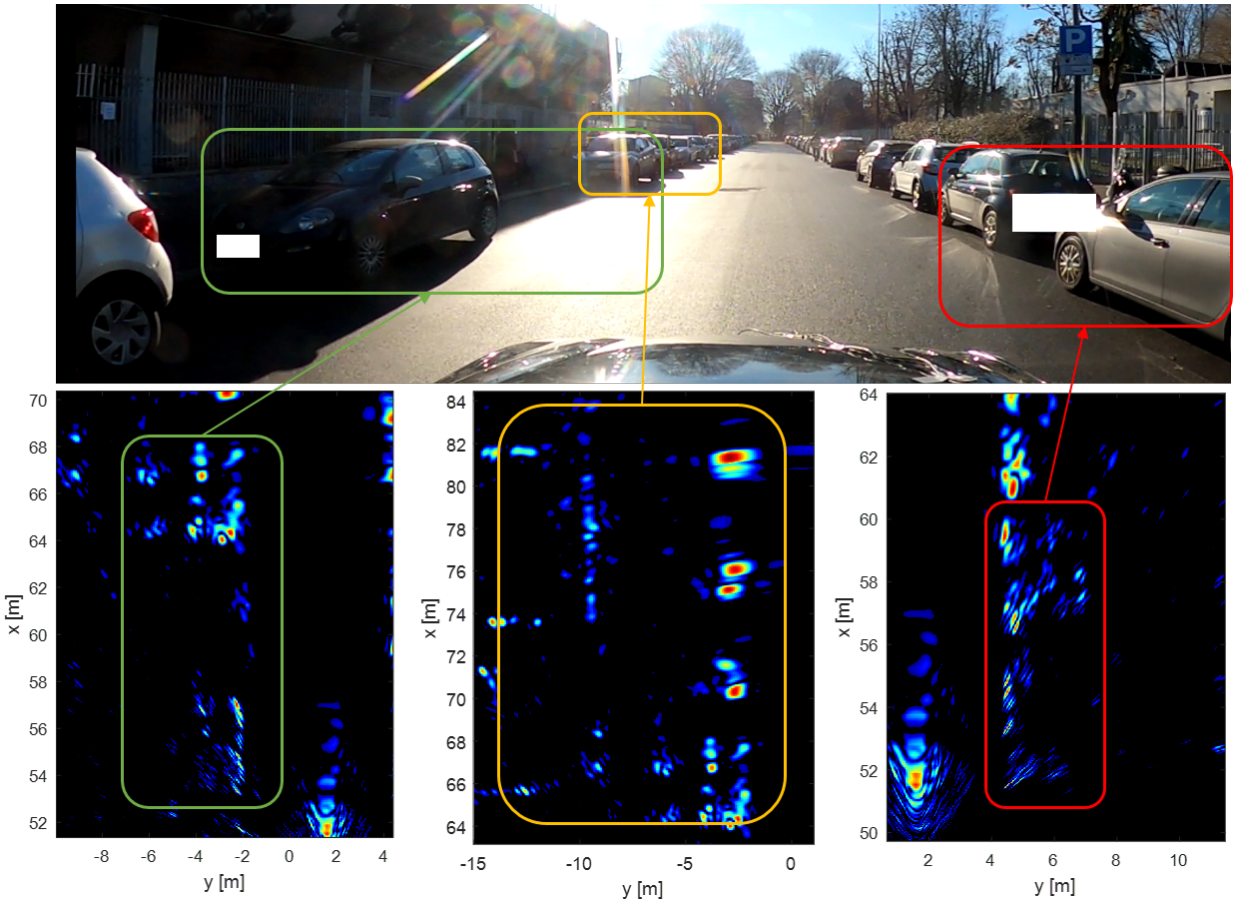

Fig. 20. (top) Optical image of the scene. (bottom left) Cars parked to the left of the moving vehicle. (center) Fence and parked cars in the far field of view. (right) Parked cars to the right of the moving vehicle. The amplitude is normalized.

based on in-car sensors are not accurate enough, as the accuracy is typically not lower than 10 cm/s.

This paper analytically derives the effect of typical residual motion estimation errors on automotive SAR focusing, setting the theoretical required accuracy on velocity estimation to avoid image degradation. In addition, we propose a complete residual motion estimation and compensation workflow based on both navigation data *and* a set of low-resolution images generated by a physical or virtual radar array mounted on the car. First, a frequency analysis is carried out over a set of static GCPs detected in the low-resolution images, retrieving the residual vehicle's velocity. The latter is then used to a phase-compensate the low-resolution images, obtaining well-focused SAR images. We evaluate the impact of errors in both the estimated target's height and angular sampling of low-resolution radar images, providing guidelines on how to properly choose GCPs. As a rule of thumb, it is recommended to choose a sparse set of GCP in far range, allowing for a better estimate of both longitudinal and transversal components of the residual velocity and minimizing the effects of a wrong focusing height of the GCPs. Moreover, the more accurate are navigation data, the more robust is the selection of GCPs against outliers, justifying the joint usage of navigation and radar data.

The entire workflow is validated using a real dataset acquired using a forward-looking MIMO radar working in W-band mounted on a vehicle moving in an open road. The proposed workflow has proven to be able to estimate centimetric velocity errors and then to correctly recover the SAR image.

APPENDIX
DEFOCUSING INDUCED BY VELOCITY ESTIMATION ERRORS

A velocity estimation error in the direction orthogonal to the line of sight of a given target (see Figure 6) induces a defocusing in the SAR image. To quantify this defocusing, let us consider a platform moving along x at a velocity v_x and a target placed at range r_0 along y, i.e., in $\mathbf{x} = [0, r_0, 0]$. The received and range compressed signal at slow time τ is, ignoring the amplitudes:

$$s_{rc}(\tau) = \exp\left\{-j\frac{4\pi}{\lambda}r(\tau)\right\} \tag{35}$$

where $r(\tau) \approx r_0 + \frac{v_x^2}{2r_0}\tau^2$ is the slow-time-varying range. Signal (35) can be represented in the Doppler frequency domain as:

$$S_{rc}(f) = \exp\left\{-j\pi\frac{f^2}{K_r}\right\} \tag{36}$$

where $K_r = 2v_x^2/(\lambda r_0)$ is usually referred to as frequency-modulation rate. A velocity estimation error along x, namely Δv_x maps into an erroneous knowledge of K_r:

$$\widehat{K}_r = \frac{2}{\lambda}\frac{(v_x + \Delta v_x)^2}{r_0} = K_r \alpha \tag{37}$$

where the scaling factor $\alpha = (1 + \frac{\Delta v_x}{v_x})^2$ accounts for the velocity estimation error. We can perform azimuth compression using a matched filter approach (which is equivalent to TDBP for the model (35)), whose frequency domain expression is:

$$H(f) = \exp\left\{+j\pi \frac{f^2}{\widehat{K}_r}\right\} \tag{38}$$

thus the azimuth compressed signal is:

$$S_{az}(f) = S_{rc}(f)H(f) = \exp\left\{-j\pi\left(\frac{\alpha - 1}{\widehat{K}_r}\right) f^2\right\} \tag{39}$$

Following the assumption of stationary phase [30], we have that the target is approximately smeared in slow-time domain by:

$$\Delta\tau = \left(\frac{\alpha - 1}{\widehat{K}_r}\right) PRF \approx 2T\frac{\Delta v_x}{v_x} \tag{40}$$

where $PRF = 2Tv_x^2/(\lambda r_0)$ is the pulse repetition frequency of the radar and $(\alpha - 1)/\widehat{K}_r \approx (\lambda r_0 \Delta v_x)/v_x^2$. The last term in (40) is equivalent to an azimuth smearing in meters of $\Delta\phi = 2T\Delta v_x$. If we impose again that the maximum smearing must not exceed one azimuth resolution cell we obtain the limits on the maximum velocity error:

$$\Delta v_\perp^{\max} = \frac{\rho_{az}^{\text{sar}}}{2T} \tag{41}$$

where ρ_{az}^{sar} is the SAR azimuth resolution for a given ϕ, and the velocity error along x has been generalized to an arbitrary orthogonal direction with respect to ϕ. Notice that (41) resembles (22), but instead of the wavelength λ we have the azimuth resolution ρ_{az}^{sar} at the numerator, thus the radial velocity error limit is much more stringent. As an example, for an observation time of $T = 130$ ms, a wavelength of $\lambda = 4$ mm and a resolution of $\rho_{az}^{\text{sar}} = 15$ cm we have $v_\perp^{\max} = 57$ cm/s, while $v_r^{\max} = 1.5$ cm/s.

ACKNOWLEDGMENT

The research has been carried out in the framework of the Huawei-Politecnico di Milano Joint Research Lab on automotive SAR. The Authors want to acknowledge Dr. Paolo Falcone from Aresys for the cooperation and support in the data acquisition campaign.

REFERENCES

[1] E. Marti, M. A. de Miguel, F. Garcia, and J. Perez, "A Review of Sensor Technologies for Perception in Automated Driving," *IEEE Intelligent Transportation Systems Magazine*, vol. 11, no. 4, pp. 94–108, 2019.

[2] J. Hasch, E. Topak, R. Schnabel, T. Zwick, R. Weigel, and C. Waldschmidt, "Millimeter-Wave Technology for Automotive Radar Sensors in the 77 GHz Frequency Band," *IEEE Transactions on Microwave Theory and Techniques*, vol. 60, no. 3, pp. 845–860, 2012.

[3] Z. Feng, M. Li, M. Stolz, M. Kunert, and W. Wiesbeck, "Lane Detection With a High-Resolution Automotive Radar by Introducing a New Type of Road Marking," *IEEE Transactions on Intelligent Transportation Systems*, vol. 20, no. 7, pp. 2430–2447, Jul. 2019. [Online]. Available: https://ieeexplore.ieee.org/document/8485664/

[4] S. Brisken, F. Ruf, and F. Höhne, "Recent Evolution of Automotive Imaging Radar and its Information Content," *IET Radar, Sonar Navigation*, vol. 12, no. 10, pp. 1078–1081, 2018.

[5] H. Iqbal, M. B. Sajjad, M. Mueller, and C. Waldschmidt, "SAR imaging in an automotive scenario," in *2015 IEEE 15th Mediterranean Microwave Symposium (MMS)*. Lecce, Italy: IEEE, Nov. 2015, pp. 1–4. [Online]. Available: http://ieeexplore.ieee.org/document/7375430/

[6] R. Feger, A. Haderer, and A. Stelzer, "Experimental verification of a 77-GHz synthetic aperture radar system for automotive applications," in *2017 IEEE MTT-S International Conference on Microwaves for Intelligent Mobility (ICMIM)*, 2017, pp. 111–114.

[7] A. Laribi, M. Hahn, J. Dickmann, and C. Waldschmidt, "Performance Investigation of Automotive SAR Imaging," in *2018 IEEE MTT-S International Conference on Microwaves for Intelligent Mobility (ICMIM)*, 2018, pp. 1–4.

[8] R. Wang, J. Pei, Y. Zhang, M. Li, Y. Huang, and J. Wu, "An Auxiliary Parking Method Based on Automotive Millimeter wave SAR," in *IGARSS 2019 - 2019 IEEE International Geoscience and Remote Sensing Symposium*. Yokohama, Japan: IEEE, Jul. 2019, pp. 2503–2506. [Online]. Available: https://ieeexplore.ieee.org/document/8898521/

[9] S. Stanko, S. Palm, R. Sommer, F. Kloppel, M. Caris, and N. Pohl, "Millimeter resolution SAR imaging of infrastructure in the lower THz region using MIRANDA-300," in *2016 European Radar Conference (EuRAD)*, 2016, pp. 358–361.

[10] D. Tagliaferri, M. Rizzi, S. Tebaldini, M. Nicoli, I. Russo, C. Mazzucco, A. V. Monti-Guarnieri, C. M. Prati, and U. Spagnolini, "Cooperative Synthetic Aperture Radar in an Urban Connected Car Scenario," in *2021 1st IEEE International Online Symposium on Joint Communications Sensing (JC S)*, 2021, pp. 1–4.

[11] T. Grebner, P. Schoeder, V. Janoudi, and C. Waldschmidt, "Radar-Based Mapping of the Environment: Occupancy Grid-Map Versus SAR," *IEEE Microwave and Wireless Components Letters*, vol. 32, no. 3, pp. 253–256, Mar. 2022. [Online]. Available: https://ieeexplore.ieee.org/document/9703257/

[12] H. Wu, "Motion Compensation for Near-Range Synthetic Aperture Radar Applications," Ph.D. dissertation, 2012.

[13] S. Tebaldini, F. Rocca, M. Mariotti d'Alessandro, and L. Ferro-Famil, "Phase Calibration of Airborne Tomographic SAR Data via Phase Center Double Localization," *IEEE Transactions on Geoscience and Remote Sensing*, vol. 54, no. 3, pp. 1775–1792, Mar. 2016. [Online]. Available: http://ieeexplore.ieee.org/document/7308057/

[14] H. Wu and T. Zwick, "A novel motion compensation algorithm for automotive SAR : Simulations and experiments," in *German Microwave Conference Digest of Papers*, 2010, pp. 222–226.

[15] H. Wu, L. Zwirello, X. Li, L. Reichardt, and T. Zwick, "Motion compensation with one-axis gyroscope and two-axis accelerometer for automotive SAR," in *2011 German Microwave Conference*, 2011, pp. 1–4.

[16] T. Gisder, F. Harrer, and E. Biebl, "Application Of A Stream-Based SAR-Backprojection Approach For Automotive Environment Perception," in *2018 19th International Radar Symposium (IRS)*, 2018, pp. 1–10.

[17] D. Tagliaferri, M. Rizzi, M. Nicoli, S. Tebaldini, I. Russo, A. V. Monti-Guarnieri, C. M. Prati, and U. Spagnolini, "Navigation-Aided Automotive SAR for High-Resolution Imaging of Driving Environments," *IEEE Access*, vol. 9, pp. 35 599–35 615, 2021.

[18] D. Wahl, P. Eichel, D. Ghiglia, and C. Jakowatz, "Phase gradient autofocus-a robust tool for high resolution SAR phase correction," *IEEE Transactions on Aerospace and Electronic Systems*, vol. 30, no. 3, pp. 827–835, Jul. 1994. [Online]. Available: http://ieeexplore.ieee.org/document/303752/

[19] A. Reigber, P. Prats, and J. Mallorqui, "Refined estimation of time-varying baseline errors in airborne SAR interferometry," *IEEE Geoscience and Remote Sensing Letters*, vol. 3, no. 1, pp. 145–149, Jan. 2006, conference Name: IEEE Geoscience and Remote Sensing Letters.

[20] P. Prats, K. A. Camara de Macedo, A. Reigber, R. Scheiber, and J. J. Mallorqui, "Comparison of Topography- and Aperture-Dependent Motion Compensation Algorithms for Airborne SAR," *IEEE Geoscience and Remote Sensing Letters*, vol. 4, no. 3, pp. 349–353, Jul. 2007. [Online]. Available: http://ieeexplore.ieee.org/document/4271465/

[21] X. Mao and D. Zhu, "Two-dimensional Autofocus for Spotlight SAR Polar Format Imagery," *IEEE Transactions on Computational Imaging*, pp. 1–1, 2016. [Online]. Available: http://ieeexplore.ieee.org/document/7574265/

[22] S. Tebaldini, T. Nagler, H. Rott, and A. Heilig, "Imaging the internal structure of an alpine glacier via l-band airborne sar tomography," *IEEE*

Transactions on Geoscience and Remote Sensing, vol. 54, no. 12, pp. 7197–7209, 2016.

[23] H. Wu and T. Zwick, "Automotive SAR for Parking Lot Detection," in *2009 German Microwave Conference*, 2009, pp. 1–8.

[24] T. Kan, G. xin, L. xiaowei, and L. zhongshan, "Implementation of Real-time Automotive SAR Imaging," in *2020 IEEE 11th Sensor Array and Multichannel Signal Processing Workshop (SAM)*, 2020, pp. 1–4.

[25] S. Gishkori, L. Daniel, M. Gashinova, and B. Mulgrew, "Imaging Moving Targets for a Forward Scanning SAR without Radar Motion Compensation," *Signal Processing*, vol. 185, p. 108110, Aug. 2021. [Online]. Available: https://linkinghub.elsevier.com/retrieve/pii/S0165168421001481

[26] D. Kellner, M. Barjenbruch, J. Klappstein, J. Dickmann, and K. Dietmayer, "Instantaneous ego-motion estimation using Doppler radar," in *16th International IEEE Conference on Intelligent Transportation Systems (ITSC 2013)*, 2013, pp. 869–874.

[27] H. Iqbal, A. Löffler, M. N. Mejdoub, D. Zimmermann, and F. Gruson, "Imaging radar for automated driving functions," *International Journal of Microwave and Wireless Technologies*, vol. 13, no. 7, pp. 682–690, Sep. 2021.

[28] A. Meta, P. Hoogeboom, and L. P. Ligthart, "Signal Processing for FMCW SAR," *IEEE Transactions on Geoscience and Remote Sensing*, vol. 45, no. 11, pp. 3519–3532, Nov. 2007. [Online]. Available: http://ieeexplore.ieee.org/document/4373378/

[29] E. C. Zaugg and D. G. Long, "Generalized Frequency Scaling and Backprojection for LFM-CW SAR Processing," *IEEE Transactions on Geoscience and Remote Sensing*, vol. 53, no. 7, pp. 3600–3614, 2015.

[30] I. G. Cumming and F. H.-c. Wong, *Digital processing of synthetic aperture radar data: algorithms and implementation*, ser. Artech House remote sensing library. Boston: Artech House, 2005, oCLC: ocm56805179.

[31] Y. Yu, M. M. d'Alessandro, S. Tebaldini, and M. Liao, "Signal Processing Options for High Resolution SAR Tomography of Natural Scenarios," *Remote Sensing*, vol. 12, no. 10, p. 1638, May 2020. [Online]. Available: https://www.mdpi.com/2072-4292/12/10/1638

[32] H. Iqbal, A. Loffler, M. N. Mejdoub, and F. Gruson, "Realistic SAR Implementation for Automotive Applications," in *2020 17th European Radar Conference (EuRAD)*, 2021, pp. 306–309.

[33] X. Gao, S. Roy, and G. Xing, "MIMO-SAR: A Hierarchical High-Resolution Imaging Algorithm for mmWave FMCW Radar in Autonomous Driving," *IEEE Transactions on Vehicular Technology*, vol. 70, no. 8, pp. 7322–7334, 2021.

[34] T. Gisder, M.-M. Meinecke, and E. Biebl, "Algorithmic Steps for SAR Backprojection on Radar Based Motion Estimation," in *2020 21st International Radar Symposium (IRS)*, Oct. 2020, pp. 385–390, iSSN: 2155-5753.

[35] H. Iqbal, M. B. Sajjad, M. Mueller, and C. Waldschmidt, "SAR Imaging in an Automotive Scenario," in *2015 IEEE 15th Mediterranean Microwave Symposium (MMS)*, 2015, pp. 1–4.

[36] Inertial Sense, *uIMU, uAHRS, uINS+RTK, uINS-Dual Calibrated Inertial Systems with Onboard GPS*, 2020.

[37] I. NovAtel, "Compact Dual Antenna SPAN Enclosure Delivers 3D Position, Velocity and Attitude," 2018.

[38] S. Duque, A. Parizzi, and F. De Zan, "Precise and Automatic 3-D Absolute Geolocation of Targets Using Only Two Long-Aperture SAR Acquisitions," *IEEE Transactions on Geoscience and Remote Sensing*, vol. 57, no. 8, pp. 5395–5406, Aug. 2019. [Online]. Available: https://ieeexplore.ieee.org/document/8673792/

[39] "AWR1243 data sheet, product information and support | TI.com." [Online]. Available: https://www.ti.com/product/AWR1243

[40] G. Akbarizadeh, "A New Statistical-Based Kurtosis Wavelet Energy Feature for Texture Recognition of SAR Images," *IEEE Transactions on Geoscience and Remote Sensing*, vol. 50, no. 11, pp. 4358–4368, Nov. 2012. [Online]. Available: http://ieeexplore.ieee.org/document/6204083/

[41] Z. Tirandaz and G. Akbarizadeh, "A Two-Phase Algorithm Based on Kurtosis Curvelet Energy and Unsupervised Spectral Regression for Segmentation of SAR Images," *IEEE Journal of Selected Topics in Applied Earth Observations and Remote Sensing*, vol. 9, no. 3, pp. 1244–1264, Mar. 2016. [Online]. Available: https://ieeexplore.ieee.org/document/7327135/

Marco Manzoni (Member, IEEE) was born in Lecco, Italy, in 1994. He received the B.Sc. (2016), M.Sc. (2018) and PhD (2022) in Telecommunication engineering from the Politecnico di Milano. His research focus on signal processing techniques for radar remote sensing including space-borne and car-borne Synthetic Aperture Radar signal processing, water vapor estimation from space-borne Interferometric SAR measurements and change detection.

Dario Tagliaferri (Member, IEEE) received the B.Sc. degree (2012), M.Sc. degree (2015) and the PhD (2019) in Telecommunication Engineering from Politecnico di Milano. He is currently a post-doctoral research fellow at Dipartimento di Elettronica, Informazione e Bioingegneria, Politecnico di Milano, Italy, in the framework of Huawei-Polimi Joint Research Lab. His research interests comprise signal processing techniques for wireless communication and sensing systems, with a particular application to vehicular scenarios. He was the recipient of the Best Paper Award from the 1st IEEE International Online Symposium on Joint Communications & Sensing 2021.

Marco Rizzi (Graduate Student Member, IEEE) received the M.S. degree in telecommunication engineering from the Politecnico di Milano, Milan, Italy, in 2019. He is currently pursuing the Ph.D. degree in information technology with the Remote Sensing Group, Politecnico di Milano. From November 2019 to November 2020, he was a Research Fellow with the Politecnico di Milano, where he was involved in the research of optimal signal processing for automotive synthetic aperture radar (SAR). His main research interest is SAR signal processing, with an emphasis on image formation for distributed SAR systems.

Stefano Tebaldini (Senior Member, IEEE) received the M.S. degree in telecommunication engineering and the Ph.D. degree from the Politecnico di Milano, in 2005 and 2009, respectively. Since 2005, he has been with the Digital Signal Processing Research Group, Politecnico di Milano, where he currently holds the position of Associate Professor.
His research activities mostly focus on Earth Observation with Synthetic Aperture Radar (SAR) and Radar design and processing. He is one of the inventors of a new technology patented by T.R.E. for the exploitation of multiple interferograms in presence of distributed scattering. He teaches courses on signal theory and remote sensing at the Politecnico di Milano. He has been involved as a key scientist in several studies by the European Space Agency (ESA) concerning the tomographic phase of BIOMASS. He was a member of the SAOCOM-CS ESA Expert Group and is currently a member of the BIOMASS MAG at ESA.

Andrea Virgilio Monti-Guarnieri (Senior Member, IEEE) received the M.Sc. degree (cum laude in electronic engineering, in 1988. He has been a Full Professor with the Dipartimento di Elettronica, Informazione e Bioingegneria, since 2017. He is the Founder of PoliMi spin-off Aresys (2003), targeting SAR, radar, and geophysics applications. He has an H index (Google) of 33, 5400 citations, received four conference awards, and holds applications for five patents. His current research interests focus on radar-based system design, calibration, MIMO, and geosynchronous SAR. He has been a reviewer of several scientific journals, Guest Editor for MPI Remote Sensing, and a member in scientific-technical committees of international workshops and symposia on Radar and Earth Observation (EO).

Claudio Maria Prati is currently a Full Professor of Telecommunications with the Electronic Department, Politecnico of Milano (POLIMI). He has chaired the Telecommunications Study Council at POLIMI. He holds five patents in the field of SAR and SAS data processing. He has been awarded three prizes from the IEEE Geoscience and Remote Sensing Society (IGARSS '89 and IGARSS '99 and best TGARSS paper 2016). He has published more than 150 papers on SAR and SAS data processing and Interferometry. He has been involved as the key scientist in several studies by the European Space Agency (ESA), the European Union (EU), the Italian National Research Council (CNR), the Italian Space Agency (ASI), and ENI-AGIP. He is the Co-Founder of Tele-Rilevamento Europa (T.R.E), a spin-off company of POLIMI that has recently become T.R.E Altamira, a CLS French group company.

Monica Nicoli (Member, IEEE) received theM.Sc. degree (cum laude) in telecommunication engineering and the Ph.D. degree in electronic and communication engineering from the Politecnico di Milano, Milan, Italy, in 1998 and 2002, respectively. She was a Visiting Researcher with ENIAgip, Italy, from 1998 to 1999, and also with Uppsala University, Sweden, in 2001. In 2002, she joined the Politecnico di Milano as a Faculty Member. She is currently an Associate Professor of Telecommunications with the Department of Management, Economics and Industrial Engineering, Politecnico di Milano, where she teaches localization, navigation and smart mobility and communication technologies for vehicles. Her research interests cover wireless communications and signal processing for ITS, with an emphasis on V2X communications, localization and navigation, cooperative and distributed systems for the Internet of Vehicles. She has coauthored 120 scientific publications (journals, conferences, and patents). She is a recipient of the Marisa Bellisario Award (1999), and a co-recipient of the Best Paper Awards of the IEEE Statistical Signal Processing Workshop (2018) and the IET Intelligent Transport Systems Journal (2014). She has served as an Associate Editor of the EURASIP Journal on Wireless Communications and Networking from 2010 to 2017, and as a Lead Guest Editor for the Special Issue on Localization in Mobile Wireless and Sensor Networks in 2011.

Ivan Russo was born in Vibo Valentia, Italy, in 1982. He received the B.Sc. degree in electronics engineering and the M.Sc. degree in telecommunications engineering from the University of Calabria, Rende, Italy, in 2003 and 2007, respectively, and the Ph.D. degree in electronics engineering from the Mediterranean University of Reggio Calabria, Reggio Calabria, Italy, in 2011, with a focus on quasi-optical (QO) amplifiers, active FSSs, and efficient array beamforming networks. From 2010 to 2011, he was with the Department of Microwave Technology, University of Ulm, Ulm, Germany, where he was involved in high-resolution near-field probes and characterization of overmoded waveguides. From 2011 to 2013, he was a University Assistant with the Institute for Microwave and Photonics Engineering, TU Graz, Graz, Austria, where he was involved in spherical near/far-field transformations, RFID antennas, and circularly and dual-polarized UWB antennas. From 2013 to 2014, he was an EMC/Antenna Engineer with Thales Alenia Space, Turin, Italy, where he was involved in installed antenna performance on satellites. From 2014 to 2018, he was an Antenna Engineer with Elettronica S.p.A., Rome, Italy, where he focused on the development of UWB antennas and phased arrays for electronic warfare applications. Since 2018, he has been with the Huawei Research Center, Milan, Italy, as an Antenna and Phased Array Engineer, where he is currently focusing on innovative automotive radar antennas and systems and advanced solution for phased arrays and high-speed interconnects.

Sergi Duque received the B.S. degree in telecommunication engineering from the Polytechnic University of Catalonia (UPC), Barcelona, Spain, in 2005. He was with UPC until 2011, where he was involved in bistatic synthetic aperture radar (SAR) and SAR interferometry. In 2008, he was with the University of Michigan, Ann Arbor, MI, USA, as a Visiting Researcher. In 2012, he joined the German Aerospace Agency, Weßling, Germany, as Researcher for the bistatic German bistatic SAR satellite mission TanDEM-X. From July 2016 to October 2019, he has been with Magna Electronics, where he has been involved in automotive radar algorithm development in close collaboration with Uhnder, bringing the first automotive digital radar to the market. From October 2018 to October 2019 he has lead the Ego Modelling algorithm team at Magna Electronics. Since November 2019, he has been working at Huawei's Research Center in Munich as automotive algorithm expert. He holds several patents in the area of automotive radar. Mr. Duque was a recipient of the Second Prize of the X Premio Rosina Ribalta given by the EPSON Foundation to the Best National Thesis Proposals in the field of information and communication technologies in 2008. He has published more than 30 papers on radar signal processing on peer reviewed conferences and journals.

Christian Mazzucco received the Laurea degree in telecommunications engineering from the University of Padova, Italy, in 2003, and the master's degree in information technology from the Politecnico di Milano, in 2004. In 2004, he joined Nokia Siemens Networks, Milan, where he was involved in research on UWB localization and tracking techniques. From 2005 to 2009, he was involved in several projects mainly researching and developing Wimax systems and high-speed LDPC decoders. In 2009, he joined Huawei Technologies, Italy, studying algorithms for high-power amplifiers digital predistortion, phase noise suppression, and MIMO for point-to-point microwave links. He is currently involved in researching phased array processing and the development of mmWave 5G BTS systems.

Umberto Spagnolini (Senior Member,IEEE) is currently a Professor of Statistical Signal Processing, the Director of Joint Lab Huawei-Politecnico di Milano, and Huawei Industry Chair. His research in statistical signal processing covers remote sensing and communication systems with more than 300 papers on peer-reviewed journals/conferences and patents. He is the author of the book Statistical Signal Processing in Engineering (J. Wiley, 2017). His specific areas of interest include mmW channel estimation and space-time processing for single/multi-user wireless communication systems, cooperative and distributed inference methods including V2X systems, mmWave communication systems, parameter estimation/tracking, focusing and wave-field interpolation for remote sensing (UWB radar and oil exploration). He was a recipient/co-recipient of Best Paper Awards on geophysical signal processing methods (from EAGE), array processing (ICASSP 2006), and distributed synchronization for wireless sensor networks (SPAWC 2007, WRECOM 2007). He is a Technical Expert of standard-essential patents and IP. He has served as a part of the IEEE Editorial boards as well as a member in technical program committees of several conferences for all the areas of interests.